

Indirect measurement of $\sin^2 \theta_W$ (or M_W) using e^+e^- pairs from γ^*/Z bosons produced in $p\bar{p}$ collisions at a center-of-momentum energy of 1.96 TeV

The CDF Collaboration
(Dated: August 17, 2015)

Drell-Yan lepton pairs are produced in the process $p\bar{p} \rightarrow e^+e^- + X$ through an intermediate γ^*/Z boson. The forward-backward asymmetry in the polar-angle distribution of the e^- as a function of the invariant mass of the e^+e^- pair is used to obtain the effective leptonic determination $\sin^2 \theta_{\text{eff}}^{\text{lept}}$ of the electroweak-mixing parameter $\sin^2 \theta_W$. The measurement sample, recorded by the Collider Detector at Fermilab (CDF), corresponds to 9.4 fb $^{-1}$ of integrated luminosity from $p\bar{p}$ collisions at a center-of-momentum energy of 1.96 TeV, and is the full CDF Run II data set. The value of $\sin^2 \theta_{\text{eff}}^{\text{lept}}$ is found to be 0.23249 ± 0.00052 , where statistical and systematic uncertainties are combined in quadrature. When interpreted within the context of the standard model using the on-shell renormalization scheme, where $\sin^2 \theta_W = 1 - M_W^2/M_Z^2$, the result yields $\sin^2 \theta_W = 0.22429 \pm 0.00050$, or equivalently a W -boson mass of 80.313 ± 0.026 GeV/ c^2 .

PACS numbers: 12.15.Lk, 13.85.Qk, 14.70.Hp

I. INTRODUCTION

In this paper, the angular distribution of charged leptons (ℓ^\pm) from the Drell-Yan [1] process is used to measure the electroweak-mixing parameter $\sin^2 \theta_W$ [2]. At the Fermilab Tevatron, Drell-Yan pairs are produced by the process $p\bar{p} \rightarrow \ell^+\ell^- + X$, where the $\ell^+\ell^-$ pair is produced through an intermediate γ^*/Z boson, and X is the hadronic final state associated with the production of the boson. In the standard model, the production of Drell-Yan lepton pairs at the Born level proceeds through two parton-level processes,

$$\begin{aligned} q\bar{q} &\rightarrow \gamma^* \rightarrow \ell^+\ell^- \text{ and} \\ q\bar{q} &\rightarrow Z \rightarrow \ell^+\ell^-. \end{aligned}$$

where the q and \bar{q} are the quark and antiquark, respectively, from the colliding hadrons. The virtual photon couples the vector currents of the incoming and outgoing fermions (f), and the spacetime structure of a photon-fermion interaction vertex is $\langle \bar{f} | Q_f \gamma_\mu | f \rangle$, where Q_f , the strength of the coupling, is the fermion charge (in units of e), and $|f\rangle$ is the spinor for fermion f . An interaction vertex of a fermion with a Z boson contains both vector (V) and axial-vector (A) current components, and its structure is $\langle \bar{f} | g_V^f \gamma_\mu + g_A^f \gamma_\mu \gamma_5 | f \rangle$. The Born-level coupling strengths are

$$\begin{aligned} g_V^f &= T_3^f - 2Q_f \sin^2 \theta_W \text{ and} \\ g_A^f &= T_3^f, \end{aligned}$$

where T_3^f is the third component of the fermion weak isospin, which is $T_3^f = \frac{1}{2}$ ($-\frac{1}{2}$) for positively (negatively) charged fermions. At the Born level, and in all orders of the on-shell renormalization scheme, the $\sin^2 \theta_W$ parameter is related to the W -boson mass M_W and the Z -boson mass M_Z by the relationship $\sin^2 \theta_W = 1 - M_W^2/M_Z^2$.

Weak-interaction radiative corrections alter the strength of the Born-level couplings into effective couplings. These effective couplings have been investigated at the Tevatron [3–5], at the LHC [6, 7], and at LEP-1 and SLD [8]. Similar couplings have been investigated with neutrino-nucleon collisions at the Tevatron [9] and with electron-proton collisions at HERA [10].

The effective $\sin^2 \theta_W$ coupling at the lepton vertex, denoted as $\sin^2 \theta_{\text{eff}}^{\text{lept}}$, has been accurately measured at the LEP-1 and SLD e^+e^- colliders. The combined average of six individual measurements yields a value of 0.23153 ± 0.00016 [8]. However, there is tension between the two most precise individual measurements: the combined LEP-1 and SLD b -quark forward-backward asymmetry ($A_{\text{FB}}^{0,b}$) yields $\sin^2 \theta_{\text{eff}}^{\text{lept}} = 0.23221 \pm 0.00029$, and the SLD polarized left-right asymmetry (\mathcal{A}_ℓ) yields $\sin^2 \theta_{\text{eff}}^{\text{lept}} = 0.23098 \pm 0.00026$. They differ by 3.2 standard deviations.

The Drell-Yan process at hadron-hadron colliders is also sensitive to the $\sin^2 \theta_{\text{eff}}^{\text{lept}}$ coupling. Measurements of the forward-backward asymmetry in the ℓ^- polar angle distribution as a function of the lepton-pair invariant mass are used to extract the coupling. This paper presents a new measurement of the $\sin^2 \theta_{\text{eff}}^{\text{lept}}$ coupling and an inference of the $\sin^2 \theta_W$ parameter using a sample of e^+e^- pairs corresponding to an integrated luminosity of 9.4 fb $^{-1}$ collected at the Tevatron $p\bar{p}$ collider. Innovative methods for the calibration of the electron energy and measurement of the forward-backward asymmetry are used. Electroweak radiative corrections used for the extraction of $\sin^2 \theta_{\text{eff}}^{\text{lept}}$ and $\sin^2 \theta_W$ are derived from an approach used at LEP-1 and SLD.

Section II provides an overview of the lepton angular distributions and the extraction of $\sin^2 \theta_{\text{eff}}^{\text{lept}}$. Section III discusses quantum chromodynamics (QCD) calculations for the forward-backward asymmetry and the inclusion

of electroweak radiative-correction form factors used in the analysis of high energy e^+e^- collisions. These form factors are important in determining $\sin^2 \theta_W$ from the measurement of $\sin^2 \theta_{\text{eff}}^{\text{lept}}$. Section IV describes the experimental apparatus. Section V reports on the selection of data for the measurement of the forward-backward asymmetry. Section VI describes the simulation of the reconstructed data. Section VII describes the corrections and calibrations applied to the data and simulation. Section VIII presents the measurement of the asymmetry and the corrections made to the data and simulation. Section IX describes the method used to extract $\sin^2 \theta_{\text{eff}}^{\text{lept}}$. Section X describes the systematic uncertainties. Section XI presents the results of this measurement using e^+e^- pairs and Finally, Sec. XII presents the summary. The units $\hbar = c = 1$ are used for equations and symbols, but standard units are used for numerical values of particle masses and momenta, e.g., 40 GeV/ c^2 and 20 GeV/ c , respectively, where c denotes the speed of light.

II. LEPTON ANGULAR DISTRIBUTIONS

The angular distribution of leptons from the Drell-Yan process in the rest frame of the boson is governed by the polarization state of the γ^*/Z boson. In amplitudes at higher order than tree level, initial-state QCD interactions of the colliding partons impart transverse momentum, relative to the collision axis, to the γ^*/Z boson. This affects the polarization states.

In the laboratory frame, the $p\bar{p}$ collision axis is the z axis, with the positive z axis oriented along the direction of the proton. The transverse component of any vector, such as the momentum vector, is defined to be relative to the z axis. The transverse component of vectors in other reference frames is defined to be relative to the z axis in those frames.

The polar and azimuthal angles of the ℓ^- direction in the rest frame of the boson are denoted as ϑ and φ , respectively. For this analysis, the ideal positive z axis coincides with the direction of the incoming quark so that the definition of ϑ parallels the definition used in e^+e^- collisions at LEP [8]. This frame is approximated by the Collins-Soper (CS) rest frame [11] for $p\bar{p}$ collisions. The rest frame is reached from the laboratory frame via two Lorentz boosts, first along the laboratory z axis into a frame where the z component of the lepton-pair momentum vector is zero, followed by a boost along the transverse component of the lepton-pair momentum vector. Within the CS frame, the z axis for the polar angle is the angular bisector between the proton direction and the reverse of the antiproton direction. The positive x axis for the azimuthal angle is along the direction of the transverse boost. A view of the CS frame is shown in Fig. 1. By construction, the CS-frame angles ϑ and φ are invariant with respect to boosts along the $p\bar{p}$ collision axis. When the transverse momentum of the lepton

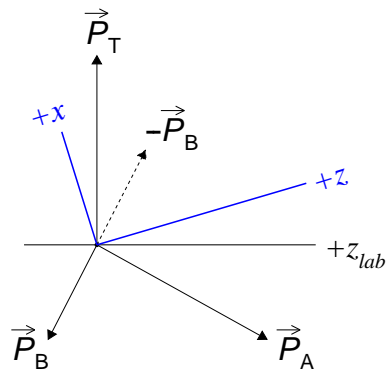


FIG. 1. Collins-Soper coordinate axes (x, z) in the lepton-pair rest frame, along with the laboratory z axis (z_{lab}). The three axes are in the plane formed by the proton (\vec{P}_A) and antiproton (\vec{P}_B) momentum vectors within the rest frame. Relative to the laboratory z axis, the transverse component of $-(\vec{P}_A + \vec{P}_B)$ is the same as the transverse-momentum vector of the lepton pair in the laboratory (\vec{P}_T).

pair is zero, the CS and laboratory coordinate-system axes are the same, and the z axis and quark directions coincide if the incoming quark of the Drell-Yan parton amplitude is from the proton.

The general structure of the Drell-Yan lepton angular distribution in the boson rest frame consists of nine helicity cross-section ratios [12]:

$$\begin{aligned} \frac{dN}{d\Omega} \propto & (1 + \cos^2 \vartheta) + \\ & A_0 \frac{1}{2} (1 - 3 \cos^2 \vartheta) + \\ & A_1 \sin 2\vartheta \cos \varphi + \\ & A_2 \frac{1}{2} \sin^2 \vartheta \cos 2\varphi + \\ & A_3 \sin \vartheta \cos \varphi + \\ & A_4 \cos \vartheta + \\ & A_5 \sin^2 \vartheta \sin 2\varphi + \\ & A_6 \sin 2\vartheta \sin \varphi + \\ & A_7 \sin \vartheta \sin \varphi. \end{aligned} \quad (1)$$

The A_{0-7} coefficients are the ratios of the helicity cross sections for boson production relative to unpolarized production, and are functions of kinematic variables of the boson. They vanish when the lepton-pair transverse momentum is zero, except for A_4 , which is present at the tree level of QCD and generates the forward-backward ℓ^- asymmetry in $\cos \vartheta$. Thus, at zero transverse momentum, the angular distribution reduces to the tree-level form $1 + \cos^2 \vartheta + A_4 \cos \vartheta$. The A_4 coefficient is relatively uniform across the range of transverse momentum where the cross section is large (under ~ 45 GeV/ c), but slowly drops for larger values of transverse momentum where the cross section is very small. The A_{5-7} coefficients appear at second order in the QCD strong coupling, α_s , and are small in the CS frame [12]. Hereafter, the angles

(ϑ, φ) and the angular coefficients A_{0-7} are specific to the CS rest frame.

The $A_4 \cos \vartheta$ term is parity violating, and is due to the interference of the amplitudes of the vector and axial-vector currents. Its presence induces an asymmetry to the φ -integrated $\cos \vartheta$ cross section. Two sources contribute: the interference between the Z -boson vector and axial-vector amplitudes, and the interference between the photon vector and Z -boson axial-vector amplitudes. The asymmetric component from the γ - Z interference cross section is proportional to g_A^f . The asymmetric component from Z -boson self-interference is proportional to a product of g_V^f from the lepton and quark vertices, and thus is related to $\sin^2 \theta_W$. At the Born level, this product is

$$T_3^\ell (1 - 4|Q_\ell| \sin^2 \theta_W) T_3^q (1 - 4|Q_q| \sin^2 \theta_W),$$

where ℓ and q denote the lepton and quark, respectively. For the Drell-Yan process, the quarks are predominantly the light quarks: u , d , or s . The coupling factor has an enhanced sensitivity to $\sin^2 \theta_W$ at the lepton- Z vertex: as $\sin^2 \theta_W \approx 0.223$, a 1% variation in $\sin^2 \theta_W$ changes the lepton factor (containing Q_ℓ) by about 8%, and it changes the quark factor (containing Q_q) by about 1.5% (0.4%) for the u (d or s) quark. Electroweak radiative corrections do not significantly alter this Born-level interpretation. Loop and vertex electroweak radiative corrections are multiplicative form-factor corrections to the couplings that change their value by a few percent.

For the description of the Drell-Yan process, the rapidity, transverse momentum, and mass of a particle are denoted as y , P_T , and M , respectively. The energy and momentum of particles are denoted as E and P , respectively. In a given coordinate frame, the rapidity is $y = \frac{1}{2} \ln[(E + P_z)/(E - P_z)]$, where P_z is the component of the momentum vector along the z axis of the coordinate frame.

The ℓ^- forward-backward asymmetry in $\cos \vartheta$ is defined as

$$A_{\text{fb}}(M) = \frac{\sigma^+(M) - \sigma^-(M)}{\sigma^+(M) + \sigma^-(M)} = \frac{3}{8} A_4(M), \quad (2)$$

where M is the lepton-pair invariant mass, σ^+ is the total cross section for $\cos \vartheta \geq 0$, and σ^- is the total cross section for $\cos \vartheta < 0$. The $\sin^2 \theta_{\text{eff}}^{\text{lept}}$ parameter is derived from the experimental measurement of $A_{\text{fb}}(M)$ and predictions of $A_{\text{fb}}(M)$ for various input values of $\sin^2 \theta_W$. From the prediction that best describes the measured value of $A_{\text{fb}}(M)$, the value of $\sin^2 \theta_{\text{eff}}^{\text{lept}}$ is derived. Electroweak and QCD radiative corrections are included in the predictions of $A_{\text{fb}}(M)$. The QCD predictions for $A_{\text{fb}}(M)$ include electroweak radiative corrections derived from an approach adopted at LEP [13].

III. ENHANCED QCD PREDICTIONS

Drell-Yan process calculations with QCD radiation do not typically include the full electroweak radiative corrections. However, the QCD, quantum electrodynamic, and weak corrections can be organized to be individually gauge invariant so that they can be applied separately and independently.

Quantum electrodynamic (QED) radiative corrections which induce photons in the final state are not included in the calculation of A_{fb} . Instead, they are included in the physics and detector simulation of the Drell-Yan process used in the measurement of A_{fb} . For the process $q\bar{q} \rightarrow \ell^+ \ell^-$, QED final-state radiation is most important and is included in the simulation. The effects of QED radiation are removed from the measured A_{fb} .

The Drell-Yan process and the production of quark pairs in high-energy e^+e^- collisions are analog processes: $q\bar{q} \rightarrow e^+e^-$ and $e^+e^- \rightarrow q\bar{q}$. At the Born level, the process amplitudes are of the same form except for the interchange of the electrons and quarks. Electroweak radiative corrections, calculated and extensively used for precision fits of LEP-1 and SLD measurements to the standard model [8], can be applied to the Drell-Yan process.

In the remainder of this section, the technique used to incorporate independently calculated electroweak radiative corrections for e^+e^- collisions into existing QCD calculations for the Drell-Yan process is presented.

A. Electroweak radiative corrections

The effects of virtual electroweak radiative corrections are incorporated into Drell-Yan QCD calculations via form factors for fermion-pair production in e^+e^- collisions, $e^+e^- \rightarrow Z \rightarrow f\bar{f}$. The Z -amplitude form factors are calculated by ZFITTER 6.43 [13], which is used with LEP-1 and SLD measurement inputs for precision tests of the standard model [8]. It is a semianalytical calculation for fermion-pair production and radiative corrections for high energy e^+e^- collisions. Corrections to fermion-pair production via the virtual photon include weak-interaction W -boson loops in the photon propagator and Z propagators at fermion-photon vertices; these corrections are not gauge invariant except when combined with their gauge counterparts in the Z amplitude. The ZFITTER weak and QED corrections are organized to be separately gauge invariant. Consequently, weak corrections to fermion-pair production via the virtual photon are included with the Z -amplitude form factors. The renormalization scheme used by ZFITTER is the on-shell scheme [14], where particle masses are on-shell, and

$$\sin^2 \theta_W = 1 - M_W^2/M_Z^2 \quad (3)$$

holds to all orders of perturbation theory by definition. Since the Z -boson mass is accurately known (to ± 0.0021

GeV/ c^2 [8]), the inference of $\sin^2 \theta_W$ is equivalent to an indirect W -boson mass measurement.

Form factors calculated by ZFITTER are stored for later use in QCD calculations. The specific standard model assumptions and parameters used in the form-factor calculation are presented in the appendix. The calculated form factors are ρ_{eq} , κ_e , κ_q , and κ_{eq} , where the label e denotes an electron and q denotes a quark. As the calculations use the massless-fermion approximation, the form factors only depend on the charge and weak isospin of the fermions. Consequently, the stored form factors are distinguished by three labels: e (electron type), u (up-quark type), and d (down-quark type). The form factors are complex valued, and are functions of the $\sin^2 \theta_W$ parameter and the Mandelstam \hat{s} variable of the $e^+e^- \rightarrow Z \rightarrow f\bar{f}$ process. The first three form factors of the amplitude are important. They can be reformulated as corrections to the Born-level g_A^f and g_V^f couplings:

$$g_V^f \rightarrow \sqrt{\rho_{eq}} (T_3^f - 2Q_f \kappa_f \sin^2 \theta_W) \text{ and} \\ g_A^f \rightarrow \sqrt{\rho_{eq}} T_3^f,$$

where $f = e$ or q .

The combination $\kappa_f \sin^2 \theta_W$, called an effective-mixing parameter, is directly accessible from measurements of the asymmetry in the $\cos \vartheta$ distribution. However, neither the $\sin^2 \theta_W$ parameter nor the form factors can be inferred from experimental measurements without assuming the standard model. The effective-mixing parameters are denoted as $\sin^2 \theta_{\text{eff}}$ to distinguish them from the on-shell definition of $\sin^2 \theta_W$ (Eq. (3)). The Drell-Yan process is most sensitive to the parameter $\sin^2 \theta_{\text{eff}}$ of the lepton vertex, $\kappa_e \sin^2 \theta_W$, which is commonly denoted as $\sin^2 \theta_{\text{eff}}^{\text{lept}}$. At the Z pole, κ_e is independent of the quark flavor. For comparisons with other measurements, the value of $\sin^2 \theta_{\text{eff}}^{\text{lept}}$ at the Z pole is taken to be $\text{Re } \kappa_e(\hat{s}_Z) \sin^2 \theta_W$ ($\hat{s}_Z = M_Z^2$).

B. QCD calculations

The Drell-Yan QCD calculations are improved by incorporating the form factors from ZFITTER into the process amplitude. This provides an enhanced Born approximation (EBA) to the electroweak terms of the amplitude. The QED photon self-energy correction is included as part of the EBA. The photon amplitude influences the shape of A_{fb} away from the Z pole via its interference with the axial-vector part of the Z amplitude. The γ - Z interference, whose cross section is proportional to $(\hat{s} - M_Z^2)$, begins to dominate the total interference cross section away from the Z pole. As the γ - Z interference dilutes measurements of $\sin^2 \theta_{\text{eff}}$, photonic corrections are also included.

The ZFITTER form factors ρ_{eq} , κ_e , and κ_q are inserted into the Born g_A^f and g_V^f couplings for the Drell-Yan process. The κ_{eq} form factor is incorporated as an amplitude correction. Complex-valued form factors are used

in the amplitude. Operationally, only the electroweak-coupling factors in the QCD cross sections are affected. The standard LEP Z -boson resonant line shape and the total decay width calculated by ZFITTER are used.

Both leading-order (LO) and next-to-leading-order (NLO) QCD calculations of A_{fb} for the process $p\bar{p} \rightarrow \gamma^*/Z \rightarrow \ell^+\ell^-$ are performed with form factors provided by ZFITTER. Two sets of parton distribution functions (PDF) are used to provide the incoming parton flux used in all QCD calculations discussed in this section except where specified otherwise. They are the NLO CTEQ6.6 [15] PDFs and the NNLO NNPDF-3.0 [16] PDFs. For consistency with the ZFITTER calculations, the NNPDFs selected are derived with a strong-interaction coupling whose value at the Z mass is 0.118.

Two NLO calculations, RESBOS [17] and the POWHEG-BOS framework [18], are modified to be EBA-based QCD calculations. For both calculations, the boson P_T^2 distribution is finite as P_T^2 vanishes. The RESBOS calculation combines a NLO fixed-order calculation at high boson P_T with the Collins-Soper-Sterman resummation formalism [19] at low boson P_T , which is an all-orders summation of large terms from gluon emission. The RESBOS calculation uses CTEQ6.6 NLO PDFs. The POWHEG-BOS calculation uses the NNLO NNPDF-3.0 PDFs, and it is a fully unweighted partonic-event generator that implements Drell-Yan production of $\ell^+\ell^-$ pairs at NLO. The NLO production implements a Sudakov form factor [20] that controls the infrared divergence at low P_T , and is constructed to be interfaced with parton showering to avoid double counting. The PYTHIA 6.41 [21] parton-showering algorithm is used to produce the final hadron-level event. The LO calculations of A_{fb} use NNPDFs for direct comparisons with the POWHEG-BOS calculations.

The RESBOS and POWHEG-BOS NLO calculations are similar and consistent when the PDFs are similar. The POWHEG-BOS NLO program, in conjunction with the NNPDF-3.0 NNLO PDFs, is chosen as the default EBA-based QCD calculation of A_{fb} with various input values of $\sin^2 \theta_W$. The RESBOS calculation is used as a reference for resummed calculations. The LO calculation serves as a reference calculation for the sensitivity of A_{fb} to QCD radiation.

IV. THE EXPERIMENTAL APPARATUS

The CDF II apparatus is a general-purpose detector [22] at the Fermilab Tevatron $p\bar{p}$ collider whose center-of-momentum (cm) energy is 1.96 TeV. The positive z -axis is directed along the proton direction. For particle trajectories, the polar angle θ_{cm} is relative to the proton direction and the azimuthal angle ϕ_{cm} is oriented about the beamline axis with $\pi/2$ being vertically upwards. The component of the particle momentum transverse to the beamline is $P_T = P \sin \theta_{\text{cm}}$. The pseudorapidity of a particle trajectory is $\eta = -\ln \tan(\theta_{\text{cm}}/2)$. Detector coordinates are specified as $(\eta_{\text{det}}, \phi_{\text{cm}})$, where

η_{det} is the pseudorapidity relative to the detector center ($z = 0$).

The central charged-particle tracking detector (tracker) is a 3.1 m long, open-cell drift chamber [23] that extends radially from 0.4 to 1.4 m. Between the Tevatron beam pipe and the central tracker is a 2 m long silicon tracker [24]. Combined, these two trackers provide efficient, high resolution tracking over $|\eta_{\text{det}}| < 1.3$. Both trackers are immersed in a 1.4 T axial magnetic field produced by a superconducting solenoid just beyond the outer radius of the drift chamber.

Outside the solenoid is the central barrel calorimeter [25, 26] that covers the region $|\eta_{\text{det}}| < 1.1$. The forward end-cap regions are covered by the end-plug calorimeters [27–29] that cover the regions $1.1 < |\eta_{\text{det}}| < 3.5$. The calorimeters are scintillator-based sampling calorimeters which are segmented along their depth into electromagnetic (EM) and hadronic (HAD) sections, and transversely into projective towers. The EM calorimeter energy resolutions measured in test beams with electrons are $\sigma/E = 14\%/\sqrt{E_T}$ for the central calorimeter, and $\sigma/E = 16\%/\sqrt{E} \oplus 1\%$ for the plug calorimeter, where the symbol \oplus is a quadrature sum, and E_T and E are in units of GeV. Both the central and plug EM calorimeters have preshower and shower-maximum detectors for electromagnetic shower identification and shower centroid measurements. The combination of the plug shower-maximum detector and silicon tracker provides enhanced tracking coverage to $|\eta_{\text{det}}| = 2.8$. However, as $|\eta_{\text{det}}|$ increases for plug-region tracks, the transverse track length within the magnetic field decreases, resulting in increasingly poorer track-curvature resolution. Within the plug shower-maximum detector, $|\eta_{\text{det}}| = 2.8$ corresponds to a radial extent from the beamline of 23 cm.

V. DATA SELECTION

The data set, collected over 2002–2011, is the full CDF Run II data set and consists of $p\bar{p}$ collisions corresponding to an integrated luminosity of 9.4 fb^{-1} . Section V A reports on the online selection of events (triggers) for the A_{fb} measurement. Section V B describes the offline selection of electron candidates, and Sec. V C describes the selection of electron pairs.

A. Triggers

Electron candidates used in the measurement of A_{fb} are selected from two online triggers: CENTRAL-18, and Z-NO-TRACK. The CENTRAL-18 selection accepts electron candidates in the central calorimeter region with $E_T > 18 \text{ GeV}$. Candidates are required to have shower clusters in the central calorimeters that are electromagnetic in nature and geometrically matched to a track from the central tracker. The Z-NO-TRACK selection accepts pairs of electron candidates located in any calorimeter region.

Each electron candidate must have a shower cluster that is electromagnetic in nature and have $E_T > 18 \text{ GeV}$. No tracking information is used in the selection. While this trigger is specifically for dielectron candidates that are both in the plug-calorimeter region, it accepts the small fraction of dielectron events that fail the CENTRAL-18 trigger.

B. Offline electron selection

To improve the purity of the sample, CDF standard central and plug [22] electron identification requirements are applied. Fiducial requirements are always applied to ensure that the electrons are in well-instrumented regions of CDF where their reconstruction is well understood and predictable. Each electron candidate is required to have an associated track. Having track matching on both electron candidates significantly reduces backgrounds. The track vertex position along the beamline (z_{vtx}) is restricted to be within the well instrumented region of CDF: $|z_{\text{vtx}}| < 60 \text{ cm}$. Overall, 3% of the $p\bar{p}$ luminous region along the beamline is outside this fiducial region.

Electron identification in the central calorimeter region is optimized for electrons of $P_T > 10 \text{ GeV}/c$. It utilizes the central and silicon trackers, the longitudinal and lateral (tower) segmentation of the EM and HAD calorimeter compartments, and the shower-maximum strip detector (CES) within the EM calorimeter. The most discriminating information is provided by the trackers in combination with the CES. An electron candidate must have shower clusters within the EM calorimeter towers and CES that have EM-like lateral shower profiles. A candidate must also have an associated track that extrapolates to the three-dimensional position of the CES shower centroid. The track transverse momentum, P_T , must be consistent with the associated electron shower E_T via an E/P selection when $P_T < 50 \text{ GeV}/c$. For both the track matching in the CES and E/P selection, allowances are included for bremsstrahlung energy loss in the tracking volume, which on average is about 20% of a radiation length. The fraction of shower energy in the HAD calorimeter towers behind the EM tower cluster must be consistent with that for electrons ($E_{\text{HAD}}/E_{\text{EM}}$ requirement). These selections are more restrictive than those applied in the online selections.

The central electron selection as described has high purity and is called the tight central electron (TCE) selection. To improve the selection efficiency of central-electron pairs used in the measurement of A_{fb} , a looser selection, called the loose central electron (LCE) selection, is applied on the second electron candidate. The LCE selection does not use transverse shower shape constraints, the E/P constraint, nor track matching in the CES. For track associations, the track need only project into the largest-energy calorimeter tower within the cluster of towers associated with the EM shower.

Electron identification in the forward plug-calorimeter

region also utilizes the trackers, the longitudinal and lateral (tower) segmentation of the EM and HAD calorimeter compartments, and the shower-maximum strip detector (PES) within the EM calorimeter. As the plug-calorimeter geometry is very different from the central geometry, the details of the selection requirements differ.

The plate-geometry, end-plug calorimeters have projective towers, but these towers are physically much smaller than the central calorimetry towers. EM showers in a plug calorimeter are clustered into “rectangular” 3×3 tower clusters in (η, ϕ) space, with the highest-energy tower in the center. The EM preshower detector is the first layer of the EM calorimeter and it is instrumented and read out separately. As there are ~ 0.7 radiation lengths of material in front of it, its energy is always included in the EM-cluster shower energy.

Tracks going into the plug calorimeters have limited geometrical acceptance in the central tracker for $|\eta_{\text{det}}| > 1.3$. The forward coverage of the silicon tracker is exploited with a calorimetry-seeded tracking algorithm called “Phoenix”. It is similar to central tracking, where tracks found in the central tracker are projected into the silicon tracker and hits within a narrow road of the trajectory seed silicon track reconstruction. With the Phoenix algorithm, the track helix in the magnetic field is specified by the position of the $p\bar{p}$ collision vertex, the three-dimensional exit position of the electron into the PES, and a helix curvature. The collision vertex is reconstructed from tracks found by the trackers. The curvature is derived from the E_T of the shower in the EM calorimeter. There are two potential helices, one for each charge. The algorithm projects each helix into the silicon tracker and seeds the silicon track reconstruction. If both projections yield tracks, the higher quality one is selected. Depending on its vertex location along the beamline, a track traverses from 0 to 8 layers of silicon. A Phoenix track is required to traverse at least three silicon layers and have at least three silicon hits. Eighty percent of the tracks traverse four or more silicon layers, and the average track acceptance is 94%.

An electron candidate in a plug calorimeter must have shower clusters within the EM calorimeter towers and PES that have EM-like lateral shower profiles, and have a longitudinal profile ($E_{\text{HAD}}/E_{\text{EM}}$) that is consistent with that for electrons. The candidate must also have an associated Phoenix track. As the track-helix curvature resolution is poor at large $|\eta_{\text{det}}|$, there is neither a P_T nor E/P selection requirement. The curvature resolution depends on the track exit position at the PES, whose radial extent relative to the beamline is 12–129 cm.

As Drell-Yan high- E_T leptons are typically produced in isolation, the electron candidates are required to be isolated from other calorimetric activity. The isolation energy, E_{iso} , is defined as the sum of E_T over towers within a 0.4 isolation cone in (η, ϕ) surrounding the electron cluster. The towers of the electron cluster are not included in the sum. For central-electron candidates, the isolation requirement is $E_{\text{iso}}/E_T < 0.1$, and for plug-

electron candidates, the requirement is $E_{\text{iso}} < 4$ GeV.

C. Offline electron pair selection

Events are required to contain two electron candidates in either the central or plug calorimeters. These events are classified into three dielectron topologies: CC, CP, and PP, where C (P) denotes that the electron is detected in the central (plug) calorimeter. As previously described in Sec. VB, electrons are required to have an associated track, pass standard selection and fiducial requirements, and be isolated from other calorimeter activity. The electron kinematic variables are based on the electron energy measured in the calorimeters and the track direction. The kinematic and fiducial regions of acceptance for electrons in the three topologies are described below.

1. Central-Central (CC)

- (a) $E_T > 25$ (15) GeV for electron 1 (2)
- (b) $0.05 < |\eta_{\text{det}}| < 1.05$

2. Central-Plug (CP)

- (a) $E_T > 20$ GeV for both electrons
- (b) Central electron: $0.05 < |\eta_{\text{det}}| < 1.05$
- (c) Plug electron: $1.2 < |\eta_{\text{det}}| < 2.8$

3. Plug-Plug (PP)

- (a) $E_T > 25$ GeV for both electrons
- (b) $1.2 < |\eta_{\text{det}}| < 2.8$

The CC topology consists of TCE-LCE combinations with asymmetric E_T selections on electrons 1 and 2. The asymmetric selection, an optimization from the previous measurement of electron angular-distribution coefficients, improves the acceptance in the electron phase space [30]. For the CP topology, the central electron candidate must pass the TCE selection. The PP-topology electron candidates are both required to be in the same end of the CDF II detector; Drell-Yan electrons of the PP topology on opposite ends of the CDF II detector are overwhelmed by QCD dijet backgrounds. In addition, the vertex locations along the beamline of the associated tracks of the candidates are required to be within 4 cm of each other.

The measurement of A_{fb} is based on the direction of the e^- in the CS frame, and any charge misidentification dilutes the measurement. Charge misidentification is very small for central tracks and significant for plug tracks. Consequently, only CC- and CP-topology pairs are used in the measurement. For the CP-topology, the central electron is used to identify the e^- . While PP-topology pairs are not directly used in the measurement of A_{fb} , they are used for plug-calorimeter calibrations and cross checks.

In this analysis, the event-weighting method described in Sec. VIII A is used to fully correct the measured A_{fb} for direct comparisons with calculations. As this method uses accepted events to correct the small increase in A_{fb} with increasing ee -pair rapidity, regions with significantly limited or no acceptance induce a bias. Consequently, the A_{fb} measurement is restricted to be within the ee -pair rapidity region with sufficient acceptance: $|y| < 1.7$.

VI. SIGNAL SIMULATION

Drell-Yan pair production is simulated using the Monte Carlo event generator, PYTHIA [31], and CDF II detector-simulation programs. PYTHIA generates the hard, leading-order QCD interaction, $q + \bar{q} \rightarrow \gamma^*/Z$, simulates initial-state QCD radiation via its parton-shower algorithms, and generates the decay $\gamma^*/Z \rightarrow \ell^+\ell^-$. The CTEQ5L [32] PDFs are used in the calculations. The underlying-event and boson- P_{T} parameters are derived from the PYTHIA configuration AW (*i.e.*, PYTUNE 101, which is a tuning to previous CDF data) [31, 33, 34].

Generated events are processed by the CDF II event and detector simulation. The detector simulation is based on GEANT-3 and GFLASH [35]. The event simulation includes PHOTOS 2.0 [36, 37], which adds final-state QED radiation (FSR) to decay vertices with charged particles (*e.g.*, $\gamma^*/Z \rightarrow ee$). The default implementation of PYTHIA plus PHOTOS (PYTHIA+PHOTOS) QED radiation in the simulation infrastructure has been validated in a previous 2.1 fb^{-1} measurement of $\sin^2 \theta_{\text{eff}}^{\text{lept}}$ using Drell-Yan electron pairs [4].

The PYTHIA calculation is further adjusted using the data and the RESBOS calculation. The generator-level P_{T} distribution is adjusted so that the shape of the reconstruction-level, simulated P_{T} distribution matches the data in two boson rapidity bins: $0 < |y| < 0.8$ and $|y| > 0.8$. For this adjustment, reconstructed ee pairs of all topologies (CC, CP, and PP) in the $66\text{--}116 \text{ GeV}/c^2$ mass region are used. The generator-level boson-mass distribution is adjusted with a mass-dependent K-factor. This K-factor is the ratio of the RESBOS boson-mass distribution calculated using CTEQ6.6 PDFs relative to the PYTHIA 6.4 [21] boson-mass distribution calculated using CTEQ5L PDFs. No kinematic restrictions are applied.

Standard time-dependent beam and detector conditions are incorporated into the simulation, including the p and \bar{p} beamline parameters; the luminous region profile; the instantaneous and integrated luminosities per data-taking period; and detector component calibrations, which include channel gains and malfunctions. The simulated events are reconstructed, selected, and analyzed in the same way as the experimental data.

VII. DATA AND SIMULATION CORRECTIONS

In this section, time and position dependent corrections and calibrations to the data and simulated data are presented. They include event rate normalizations of the simulation to the data, energy calibrations of both the data and simulation, and the modeling and removal of backgrounds from the data. There are 1 440 EM calorimeter towers, each of which can have different responses over time and position. Many aspects are correlated, and the overall correction and calibration process is iterative.

A. Event rate normalizations

The CDF II detector-simulation program does not model the trigger and reconstruction efficiencies observed in the data with sufficient precision. There are time, detector location, and luminosity dependent differences. To correct the observed differences in rate between the data and simulation, a scale-factor event weight is applied to simulated events. The scale factor is the ratio of the measured efficiencies of the data to the simulation versus time, detector location, and instantaneous luminosity.

The base correction using measured efficiencies is inadequate for the A_{fb} measurement. There are two reasons: a) due to the limited statistics of the data, the bin sizes for the time, position, and luminosity dependence are wide, and a finer resolution is needed, and b) the Tevatron $p\bar{p}$ luminosity profile is difficult to simulate. The second-level correction uses event-count ratios between the data and simulation, or scale factors, as the event weight. Events are required to pass all selection requirements and the ee -pair mass is required to be within the $66\text{--}116 \text{ GeV}/c^2$ range. Events are separated in the CC, CP, and PP topologies and corrected separately.

The time and luminosity dependencies are related. The distributions of the number of $p\bar{p}$ collision vertices in each event (n_{vtx}) and the location of these vertices along the beamline (z_{vtx}) changed significantly with improvements to the Tevatron collider. These distributions are inadequately simulated and corrected separately. For the n_{vtx} correction, the data and simulation are grouped into 39 calibration periods, and the distribution corrected on a period-by-period basis. The correction of the z_{vtx} distribution is split into a smaller set of seven time blocks corresponding to improvements in the Tevatron collider. This distribution needs to be simulated well because at large $|z_{\text{vtx}}|$, the electron acceptance in E_{T} changes significantly.

The second-level correction to remove detector location dependencies is a function of $|\eta_{\text{det}}|$. In the central calorimeter, the corrections are limited and small. In the plug calorimeters, the corrections are larger and they correct the effects of tower response differences between the actual calorimeter and the simulated calorimeter near

tower boundaries.

B. Energy calibrations

Electron energy calibrations are multicomponent calibrations, and it is infeasible to calibrate all components simultaneously. Instead, components are calibrated in smaller independent groups and the process iterated. Both relative and absolute calibrations are utilized to calibrate the data and the simulation.

All electron-pair topologies are used for calibrations, and there are two independent data sets that can provide a full set of calibrations: CC+PP events, and CP events. Electron pairs used in the calibration must satisfy the selection requirements. Both electron energy and ee -pair mass (M_{ee}) distributions can be used. For positional calibrations, one of the electrons, denoted as the reference, provides the detector coordinates ($\eta_{\text{det}}, \phi_{\text{cm}}$); the partner electron is allowed to be anywhere in the detector so that miscalibrations of the current iteration are averaged out. Both electrons of the pair are used as the reference. The sharp, nearly symmetric peak at the Z -pole of the M_{ee} distribution is required for the fine tuning of the calibrations. The energy distribution is not ideal for tuning because the distribution tends to be broad and asymmetric, and its shape is dependent on the kinematics of the partner electron.

Absolute energy calibrations are based on three electron-pair mass distributions: a) generator level, b) simulated data, and c) data. The mass distributions are fit to a mass line shape that includes the Z -pole mass as a fit parameter. The data and simulated data Z -pole mass values are calibrated to the generator-level Z -pole mass value [38].

Generator-level events are selected by requiring that their kinematics after detector simulation pass all selection criteria. The generator-level mass is after QED FSR and is evaluated using clustered energies. The FSR electrons and photons are clustered about the seed tower in a manner similar to the clustering of electron reconstruction. The seed tower is based on the reconstructed electron, and the projection from the $p\bar{p}$ collision vertex to the tower is via the track helix.

The generator-level mass distribution is fit to the standard LEP Z -boson resonant line shape. The data and simulation mass distributions are fit to the standard LEP Z -boson resonant line shape convoluted with the Gaussian resolution functions of the calorimeters. The Z -pole mass and resolution width values are allowed to vary but the resonant width is fixed to the corresponding generator-level fit value. With this method, the resolution width values of the simulation and data are directly comparable and are used to calibrate central and plug electron energy resolutions of the simulation to the data. Typically, the fit region is $\pm 5 \text{ GeV}/c^2$ around the Z peak.

The first step in an iteration is the time-dependent calibration of the overall absolute-energy scales for the

central and plug calorimeters. These corrections are for each of the 39 calibration periods introduced in the previous section.

The next step is the relative-energy calibrations for individual calorimetry towers and the response maps within their boundaries. The energy response is measured with the average of the scaled mass $M_{ee}/(91.15 \text{ GeV}/c^2)$ over 0.9–1.1. The corrections are based on the ratio of the energy response to the overall average. These corrections are important in the high $|\eta_{\text{det}}|$ region of the plug calorimeters where standard calibrations are difficult. The corrections are split into two time periods: calibration periods 0–17 and 18–39. Period 18 is the start of stable and consistent Tevatron operations. Both the central and plug calorimeter towers required additional response map tuning at the periphery of the towers.

The third step is an absolute-energy calibration over the η -tower rings of the central and plug calorimeters. Towers from both ends of the detector are combined. There are 22 η -tower rings, and 20 are in the acceptance region. The calibration is split into two time periods: 0–17 and 18–39. Separate calibrations are maintained for CC+PP and CP data. The calibration is done in two passes and is iterative. First, the central and plug rings are calibrated with events from the CC+PP data. These calibrations are used only for CC- and PP-topology pairs. Then the CP data set calibration is derived from a combination of the CC+PP and CP data.

The underlying-event energy correction accompanies the η -ring correction. The M_{ee} distributions have an observable variation with the number of $p\bar{p}$ collision vertices in an event. Using the ansatz that the underlying-event energy per shower increases linearly with n_{vtx} , these mass distributions are used to extract the underlying-event energy of an electron shower per vertex for each η ring. For the central calorimeter, the value is approximately constant and has a value of approximately 35 MeV. For the plug calorimeters, the value is approximately 150 MeV for $|\eta_{\text{det}}| < 2$ and increases to 1.5 GeV at $|\eta_{\text{det}}| \sim 2.8$.

The fourth step is an absolute-energy calibration over a grid with 16 η_{det} and eight ϕ_{cm} bins. The η_{det} bins span both ends of the detector, and the inner eight bins are for the central calorimeter, and the outer eight for the plug calorimeters. The $(\eta_{\text{det}}, \phi_{\text{cm}})$ bins are further divided into same-side (SS) and opposite-side (OS) pairs: SS-pair electrons have η_{det} values with the same sign and OS-pair electrons have different signs. There are few tenths of a percent differences between the SS- and OS-pair calibrations. The z_{vtx} distribution of $p\bar{p}$ collisions has a rms of 30 cm, and as $|z_{\text{vtx}}|$ increases to large values, the shower-geometry and response to electrons in the calorimeters change.

The energy resolution of the calorimeter simulation are also adjusted for the calibration bins of the fourth step. Line-shape fits to the M_{ee} distributions of the data and the simulation provide the resolution-smearing parameters σ_d^2 and σ_s^2 of the data and simulation, respectively.

For most bins, the resolution is adjusted by adding in quadrature, additional Gaussian smearing with an rms of this value: $\sigma_d^2 - \sigma_s^2$. For 24% of the central bins, this value is negative. For these bins, the only feasible option is to reduce the simulation energy bias $\Delta E_{\text{bias}} \equiv E_{\text{gen}} - E_{\text{rec}}$, where E_{gen} is the generator-level clustered energy and E_{rec} is the reconstruction-level energy. The resolution is modified on an event-by-event basis by scaling the bias with the factor f_{bias} : $E'_{\text{rec}} = E_{\text{gen}} - f_{\text{bias}} \Delta E_{\text{bias}}$, where E'_{rec} is the new reconstruction-level energy. The smallest value of f_{bias} is 0.83.

C. Backgrounds

The backgrounds are negligible in the Z -peak region used for the energy calibration but they are significant in the low and high mass regions of the M_{ee} distributions for the data. In this section, the level and shapes of the backgrounds in the ee -pair mass distribution are determined separately for each of the CC, CP, and PP topologies.

The backgrounds are from QCD and the electroweak (EWK) processes of WW , WZ , ZZ , $t\bar{t}$, W +jets, and $Z \rightarrow \tau^+\tau^-$. The WW , WZ , and ZZ backgrounds are collectively denoted as the diboson background. The EWK-process backgrounds are derived from PYTHIA [31] samples that are processed with the CDF II detector simulation, and in which the integrated luminosity of each sample is normalized to that for the data. The diboson and $t\bar{t}$ samples are NLO simulations. As the W +jets and $Z \rightarrow \tau^+\tau^-$ processes are LO simulations, the total cross section used for the calculation of the integrated luminosity includes a NLO-to-LO K-factor of 1.4. Events of the EWK-process sample are required to pass all selections required of the data.

The QCD background is primarily from dijets that are misidentified as electrons. This background is derived from the data by postulating that the difference between the observed M_{ee} distribution and the sum of the simulated data and EWK-process backgrounds is the QCD background. Operationally, the QCD level and shape are parameters in a fit of the simulated data, EWK-process backgrounds, and QCD background to the data. The mass range for the fit is 42–400 GeV/ c^2 with 50 equally spaced bins in $\ln M_{ee}$, and the minimization statistic is the χ^2 between the data and the sum of predicted components over all bins. The normalizations of the simulated data and EWK-process backgrounds are allowed to vary from their default values via unit-normalized scale factors. However, several EWK-process backgrounds are only allowed to vary within their normalization uncertainties. The constraint is implemented with an additional χ^2 term $(f_{\text{norm}} - 1)^2 / 0.085^2$, where f_{norm} is the scale factor of the background and 0.085 is the estimate of the uncertainty. The very small $t\bar{t}$, diboson, and W +jets backgrounds are in this group.

The QCD sample for background subtractions is de-

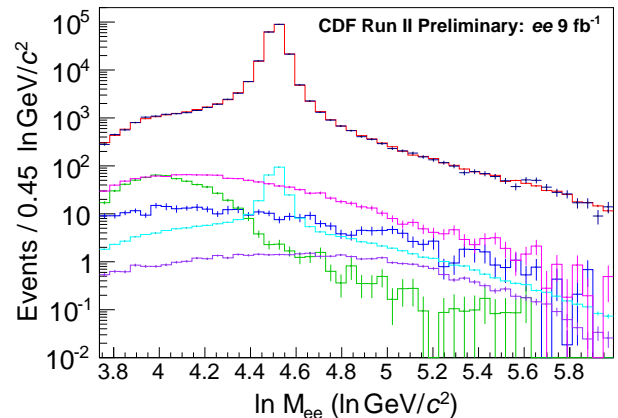


FIG. 2. CC-topology oppositely charged M_{ee} distributions. The (black) crosses are the data, the (red) histogram overlapping the data is the sum of all components, the (green) histogram concentrated at lower masses is the $Z \rightarrow \tau^+\tau^-$ component, and the (cyan) histogram in the middle with the Z peak is the diboson component. The remaining broad distributions, from top to bottom are: QCD (magenta), W +jets (blue), and $t\bar{t}$ (purple). The comparison of the data with the sum of the components yields a χ^2 of 56 for 50 bins.

rived from the same electron-data sample used for the A_{fb} measurement. Two electron-like candidates are selected by reversing criteria that suppress hadrons and QCD jets. One candidate is required to pass all electron selection requirements except the isolation criterium. The other is required to be “jet-like” by reversing the isolation and $E_{\text{had}}/E_{\text{em}}$ selection criteria. As the reversed selection criteria biases the M_{ee} distribution, events of the QCD sample are reweighted so that the overall normalization and the shape of the M_{ee} distribution matches those extracted from the procedure described above.

For the CC topology, events are separated into same-charge and opposite-charge pairs, and both distributions are fit simultaneously for the background parameters. As the same-charge distribution is highly enriched with QCD events (50–60% in the low and high mass regions), the default level and shape for the QCD background is extracted from this distribution. The default $Z \rightarrow \tau^+\tau^-$ normalization is not accommodated by the data and the other components. If the $Z \rightarrow \tau^+\tau^-$ normalization is allowed to vary, the fit value of its scale factor is 0.53 ± 0.11 . However, if the normalization is constrained to its default, the fit value of its scale factor is 0.83 ± 0.07 and the χ^2 is larger by 6 units relative to the freely varying normalization. Consequently, the 0.53 value is chosen for the A_{fb} measurement and the 0.83 value is applied towards the systematic uncertainty. The CC-topology opposite-charge M_{ee} distributions for the data and the component parts are shown in Fig. 2.

For the CP and PP topologies, a background enriched sample that passes selection requirements is not available. The level of the QCD background in the signal sample is too small for a robust determination of both

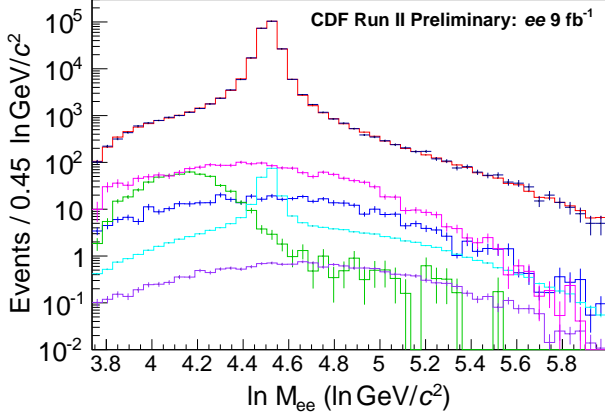


FIG. 3. CP-topology M_{ee} distributions. The (black) crosses are the data, the (red) histogram overlapping the data is the sum of all components, the (green) histogram concentrated at lower masses is the $Z \rightarrow \tau^+\tau^-$ component, and the (cyan) histogram in the middle with the Z peak is the diboson component. The remaining broad distributions, from top to bottom are: QCD (magenta), W +jets (blue), and $t\bar{t}$ (purple). The comparison of the data with the sum of the components yields a χ^2 of 50 for 50 bins.

its shape and level in all mass regions. As this affects the normalizations of the other background components, the $Z \rightarrow \tau^+\tau^-$, W +jets, diboson, and $t\bar{t}$ components are constrained to their default normalizations. Since the QCD-sample mass distribution is well described by an asymmetric-Gaussian function, it is used for the parametrization of the QCD background within the signal samples. The function consists of two Gaussian functions with different rms values but with common mean values. They are joined at the value of their common mean. However, this function is too flexible for a stable and reasonable determination of the QCD background in both the low and high mass regions. For the CP topology, the high-side rms of the asymmetric-Gaussian is optimized manually, and for the PP topology, the mean of the asymmetric-Gaussian is manually optimized. The CP- and PP-topology M_{ee} distributions for the data and the component parts are shown in Figs. 3 and 4, respectively.

The CC-, CP-, and PP-topology samples contain 226 616, 258 233, and 79 698 events, respectively, within the 42–400 GeV/c^2 mass region. Table I summarizes the overall background levels for these samples. The total background for CC-, CP-, and PP-topology samples are 1.1%, 1.2%, and 2.1%, respectively. However, in the low and high mass regions, the background levels are larger. For electron pairs of the CC topology, it is about 3%, and for the CP topology, it is about 5%. The PP sample is only used for calibrations.

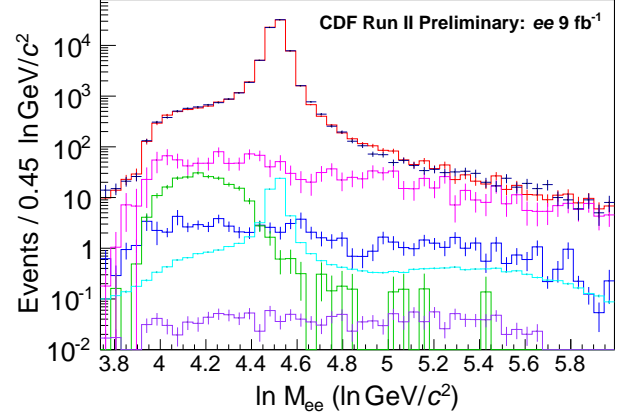


FIG. 4. PP-topology M_{ee} distributions. The (black) crosses are the data, the (red) histogram overlapping the data is the sum of all components, the (green) histogram concentrated at lower masses is the $Z \rightarrow \tau^+\tau^-$ component, and the (cyan) histogram in the middle with the Z -peak is the diboson component. The remaining broad distributions, from top to bottom are: QCD (magenta), W +jets (blue), and $t\bar{t}$ (purple). The comparison of the data with the sum of the components yields a χ^2 of 69 for 50 bins.

TABLE I. Background fractions within the 42–400 GeV/c^2 mass region.

Component	Background Fraction (%)		
	CC	CP	PP
QCD	0.55	0.69	1.64
$Z \rightarrow \tau\tau$	0.26	0.21	0.27
W +jets	0.13	0.16	0.10
Diboson	0.14	0.10	0.08
$t\bar{t}$	0.02	0.01	0.01

VIII. THE A_{fb} MEASUREMENT

The Collins-Soper frame angle, $\cos\vartheta$ [11], is reconstructed using the following laboratory-frame quantities: the lepton energies, the lepton momenta along the beam line, the dilepton invariant mass, and the dilepton transverse momentum. The angle of the negatively charged lepton is

$$\cos\vartheta = \frac{l_+^- l_-^+ - l_-^- l_+^+}{M\sqrt{M^2 + P_T^2}},$$

where $l_{\pm} = (E \pm P_z)$ and the $+$ ($-$) superscript specifies that l_{\pm} is for the positively (negatively) charged lepton. Similarly, the Collins-Soper expression for φ in terms of laboratory-frame quantities is

$$\tan\varphi = \frac{\sqrt{M^2 + P_T^2}}{M} \frac{\vec{\Delta} \cdot \hat{R}_T}{\vec{\Delta} \cdot \hat{P}_T},$$

where $\vec{\Delta}$ is the difference between the ℓ^- and ℓ^+ momentum vectors; \hat{R}_T is the transverse unit vector along

$\vec{P}_p \times \vec{P}$, with \vec{P}_p being the proton momentum vector and \vec{P} the lepton-pair momentum vector; and \hat{P}_T is the unit vector along the transverse component of the lepton-pair momentum vector. At $P_T = 0$, the angular distribution is azimuthally symmetric.

The A_{fb} is measured in 15 mass bins, starting with $M = 50 \text{ GeV}/c^2$. This section details the measurement method, and presents the fully corrected measurement. Section VIII A describes a newly developed event-weighting technique. Section VIII B describes final calibrations and presents comparisons of the data and simulation. Section VIII C describes the resolution-unfolding technique and the corresponding covariance matrix of the unfolded A_{fb} measurement. Section VIII D describes the final corrections to the measurement and presents the fully corrected measurement of A_{fb} .

A. Event-weighting method

The forward-backward asymmetry A_{fb} of Eq. (2) is typically determined in terms of the measured cross section $\sigma = N/(\mathcal{L}\epsilon A)$, where N is the number of observed events after background subtraction, \mathcal{L} is the integrated luminosity, ϵ the reconstruction efficiency, and A the acceptance within the kinematic and fiducial restrictions. The expression is

$$A_{fb} = \frac{N^+ / (\epsilon A)^+ - N^- / (\epsilon A)^-}{N^+ / (\epsilon A)^+ + N^- / (\epsilon A)^-}.$$

The terms $N^{+(-)}$ and $(\epsilon A)^{+(-)}$ respectively represent N and ϵA for candidates with $\cos \vartheta \geq 0$ ($\cos \vartheta < 0$).

The A_{fb} is measured using a novel and simpler technique: the *event-weighting* method [39]. The method is equivalent to measurements of A_{fb} in $|\cos \vartheta|$ bins with these simplifying assumptions:

1. $(\epsilon A)^+ = (\epsilon A)^-$ in each $|\cos \vartheta|$ bin, and
2. Equation (1) describes the angular distributions.

The measurement of A_{fb} within a $|\cos \vartheta|$ bin (A'_{fb}) only depends on N^\pm , but is related to A_{fb} through an angular dependence,

$$A'_{fb} = \frac{N^+ - N^-}{N^+ + N^-} \propto A_{fb} \frac{|\cos \vartheta|}{1 + \cos^2 \vartheta + \dots}, \quad (4)$$

where $1 + \cos^2 \vartheta + \dots$ denotes symmetric terms in Eq. (1). The $|\cos \vartheta|$ term arises from the difference in the numerator $N^+ - N^-$, and the $1 + \cos^2 \vartheta + \dots$ term arises from the sum in the denominator $N^+ + N^-$. As the angular factor is the equivalent of an importance-sampling function of Monte Carlo simulations, the binned measurements are reformulated into an unbinned, event-by-event weighted expression

$$A_{fb} = \frac{N_n^+ - N_n^-}{N_d^+ + N_d^-}. \quad (5)$$

The N_n^\pm and N_d^\pm terms represent weighted event counts, and the subscripts n and d signify the numerator and denominator sums, respectively, which contain the same events but with different event weights. The weights take into account the angular terms of the numerator and denominator sums, and include a statistical factor for the expected measurement uncertainty at each value of $|\cos \vartheta|$, the inverse of the square of the angular factor in A'_{fb} . Consequently, the method is equivalent to using a maximum-likelihood technique, and for an ideal detector, the statistical precision of A_{fb} is expected to be about 20% better relative to the direct counting method [39]. However, detector resolution and limited acceptance degrade the ideal gain.

The event weights are functions of the reconstructed kinematic variables, $\cos \vartheta$, φ , and the lepton-pair variables, M and P_T . Only the A_0 and A_2 terms of Eq. (1) are used in the denominator of the angular factor of Eq. (4), and the angular coefficients are parametrized with

$$A_0 = A_2 = \frac{k P_T^2}{k P_T^2 + M^2},$$

where k is a tuning factor for the P_T dependence of the A_0 and A_2 coefficients. For this analysis, $k = 1.65$, which is derived from a previous measurement of angular coefficients [30]. The exact form of these angular terms in the event weights is not critical for A_{fb} because the bulk of the events is at low boson P_T .

The EWK and QCD backgrounds are subtracted from the weighted event sums on an event-by-event basis. Background events from the EWK and QCD samples are assigned negative event weights when combined with the event sums.

The event-weighting method does not compensate the following sources of bias:

1. smearing of kinematic variables due to the detector resolution,
2. kinematic regions with limited acceptance, and
3. detector nonuniformity resulting in $(\epsilon A)^+ \neq (\epsilon A)^-$.

Resolution-smearing effects are unfolded with the aid of the simulation. For the unfolding to be accurate, the electron energy scale and resolution for both the data and simulation are precisely calibrated. In addition, the $\cos \vartheta$ and electron-pair invariant-mass distributions of the simulation are matched to agree with the data.

After resolution unfolding, the event-weighted A_{fb} can have a small, second-order bias. The bias is estimated using the simulation and is the difference between the true value of A_{fb} from the physics events generated by PYTHIA and the result of the measurement on the simulated sample. One source of bias is from the limited electron-pair acceptance at forward rapidities. There is a small increase in the forward-backward physics asymmetry with increasing $|y|$ for $|y| \approx 1$ and above. As the

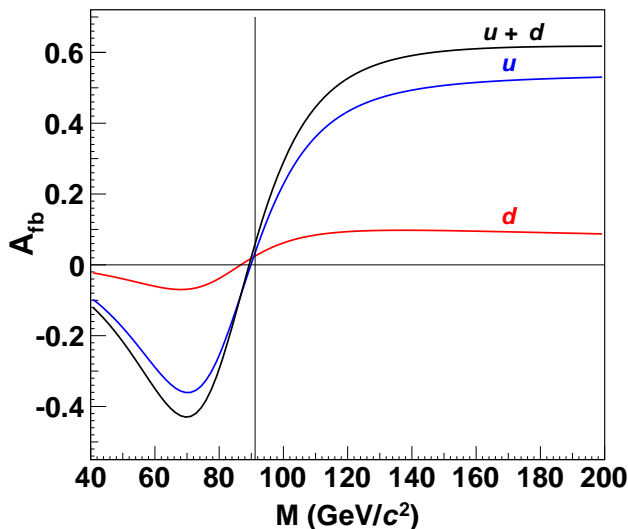


FIG. 5. Expected dependence of A_{fb} as a function of the lepton-pair invariant mass M . The vertical line is at $M = M_Z$. The label $u+d$ denotes the overall asymmetry. The labels u and d denote the contributions of charge $2/3$ and $-1/3$ quarks, respectively, to the overall asymmetry.

event-weighted A_{fb} is an average of A_{fb} over the y distribution of accepted events, regions with significantly limited or no acceptance bias the average. The kinematic restriction of $|y| < 1.7$ specified in Sec. VC limits this bias. Another possible source of bias is from detector nonuniformity: $(\epsilon A)^+ \neq (\epsilon A)^-$. This distorts the estimate of A'_{fb} [Eq. (4)]. The effects of these biases, which are quantified later in Sec. VIID, are removed from the A_{fb} measurement.

B. Final calibrations

The typical dependence of A_{fb} as a function of the lepton-pair invariant mass (M) is shown in Fig. 5. The offset of A_{fb} from zero at $M = M_Z$ is related to $\sin^2 \theta_W$. However, the increase in magnitude of A_{fb} away from the Z pole is a consequence of γ - Z interference, and is related to PDFs. Measurements of A_{fb} as a function of M simultaneously probe $\sin^2 \theta_W$ and the PDFs.

The slope and the intercept of A_{fb} is distorted by detector miscalibrations. With energy miscalibrations, an event produced at mass M with asymmetry $A_{fb}(M)$ is associated with a different mass M' . The measured $A_{fb}(M')$ becomes biased because of this systematic dilution. This affects both the data and the simulation. Energy resolution miscalibrations in the simulation affect the unfolding of the resolution smeared $A_{fb}(M)$ and induce additional measurement biases.

The Collins-Soper $\cos \vartheta$ distribution for the simulation is also adjusted to improve agreement with the data. Only the symmetric part of the distribution is adjusted.

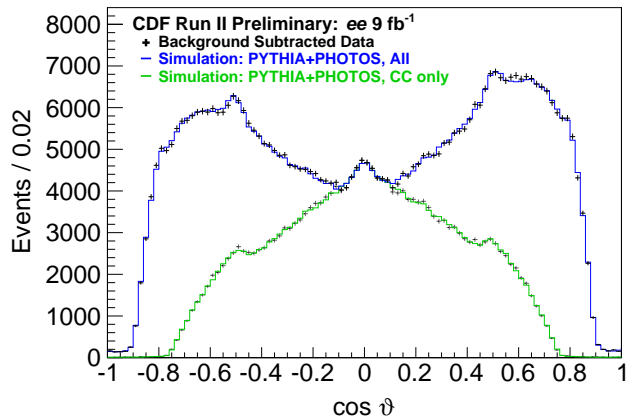


FIG. 6. $\cos \vartheta$ distributions in the Collins-Soper frame for dielectrons with $66 < M_{ee} < 116 \text{ GeV}/c^2$: the crosses are the background-subtracted data and the histograms are simulated data. The upper pair of crosses and histogram is from the combination of the CC and CP topologies, and the lower pair is the contribution from the CC topology.

The adjustments, determined for six electron-pair invariant mass bins whose boundaries are aligned with those used in the measurement, are determined from the ratios of the data-to-simulation $\cos \vartheta$ distributions. The ratios are projected onto the first five Legendre polynomials: $\Sigma_{i=0}^{i=4} p_i P_i(\cos \vartheta)$, where p_i are projection coefficients and $P_i(\cos \vartheta)$ are Legendre polynomials. The ratios are normalized so that the event count in the mass bin matches that of the data. The symmetric parts of the projections describe the ratios well and are used as the adjustments. Separate adjustments are applied to the CC- and CP-topology electron pairs as event weights. The corrections are a few percent or less in regions where the acceptance is large.

Figure 6 shows the $\cos \vartheta$ distributions after the adjustments for the combination of the CC and CP topologies and for the CC topology alone. The CP-topology dielectrons are dominant at large $|\cos \vartheta|$ and its contribution in that region significantly reduces the statistical uncertainty of this A_{fb} measurement. Figure 7 shows the Collins-Soper φ distribution.

Each calibration, including the angular-distribution calibration, can affect the others. The final result is after a series of iterations. The CC-topology electron-pair mass distribution in the range of 66 – $116 \text{ GeV}/c^2$ is shown in Fig. 8. The CP-topology electron-pair mass distribution in the same range is shown in Fig. 9. The PP-topology dielectrons are only used in the calibration, and over the electron-pair mass range of 66 – $116 \text{ GeV}/c^2$, the comparison of the simulation with the data yields a χ^2 of 232 for 200 bins.

The mass distribution of CC same-charge dielectrons has a clear Z -boson peak from charge misidentification. Figure 10 shows the CC same-charge mass distribution of the data and the simulation. This figure confirms that

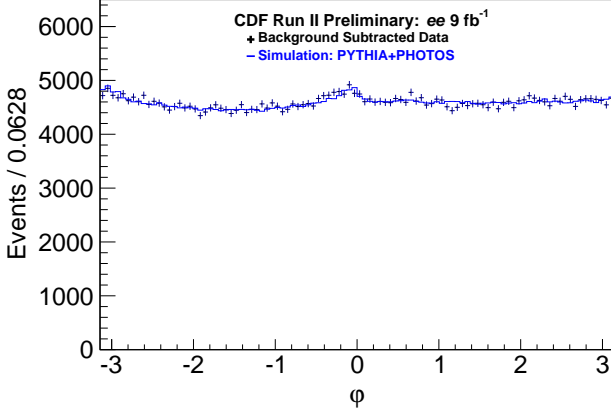


FIG. 7. φ distribution in the Collins-Soper frame for CC- and CP-topology dielectrons with $66 < M_{ee} < 116 \text{ GeV}/c^2$. The crosses are the background-subtracted data and the solid histogram is from the simulation.

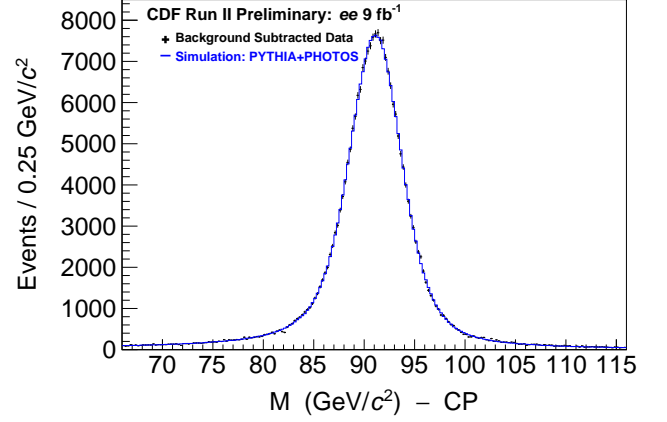


FIG. 9. CP electron-pair invariant mass distribution. The crosses are the background-subtracted data and the solid histogram is from the simulation. The comparison of the simulation with the data yields a χ^2 of 235 for 200 bins.

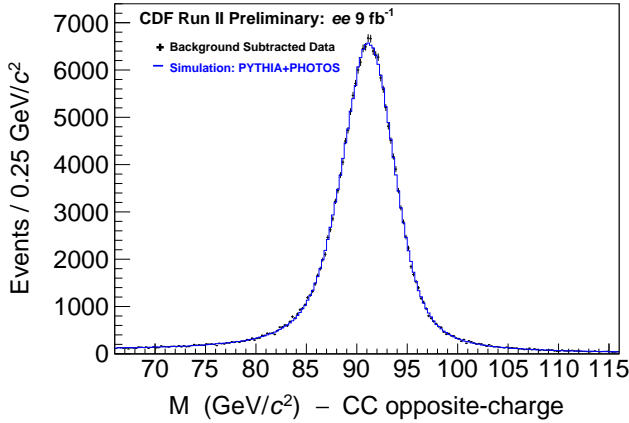


FIG. 8. CC opposite-charge ee -pair invariant mass distribution. The crosses are the background-subtracted data and the solid histogram is from the simulation. The comparison of the simulation with the data yields a χ^2 of 214 for 200 bins.

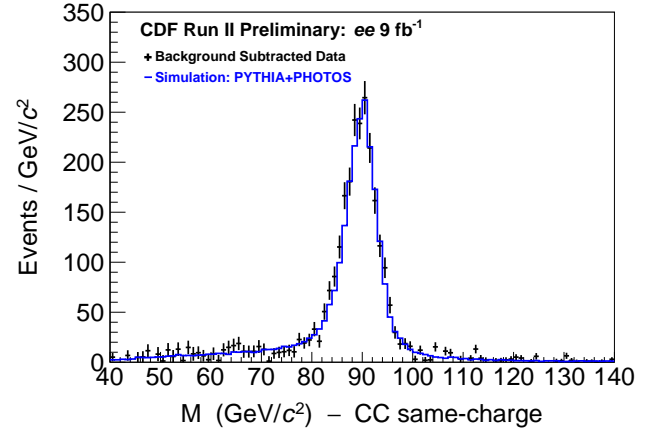


FIG. 10. CC same-charge ee -pair invariant mass distribution. The crosses are the background-subtracted data and the solid histogram is from the simulation.

charge misidentification is reproduced well by the detector simulation. Charge misidentification on the central electron of CP pairs is thus expected to be well simulated.

The electron E_T distributions of the data are reasonably well described by the simulation. Figure 11 shows the larger E_T distribution of CC-topology electrons for both the data and the simulation. Figure 12 shows the larger E_T distribution of CP-topology electrons, which can either be the central or plug electron.

C. Resolution unfolding

After applying the calibrations and corrections to the experimental and simulated data, the A_B is measured in bins of the electron-pair invariant mass with the event-weighting method. This measurement is denoted as

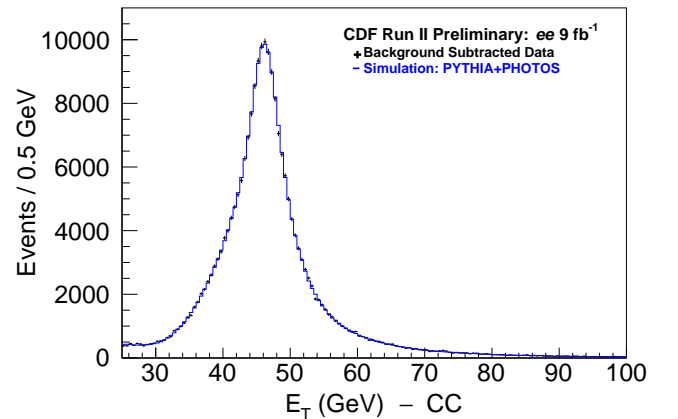


FIG. 11. E_T distribution for the CC-topology electron with the larger E_T . The crosses are the background-subtracted data and the solid histogram is from the simulation.

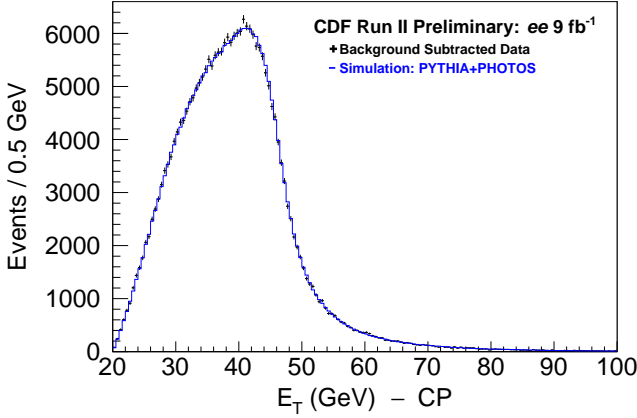


FIG. 12. E_T distribution for the CP-topology electron with the larger E_T . The crosses are the background-subtracted data and the solid histogram is from the simulation.

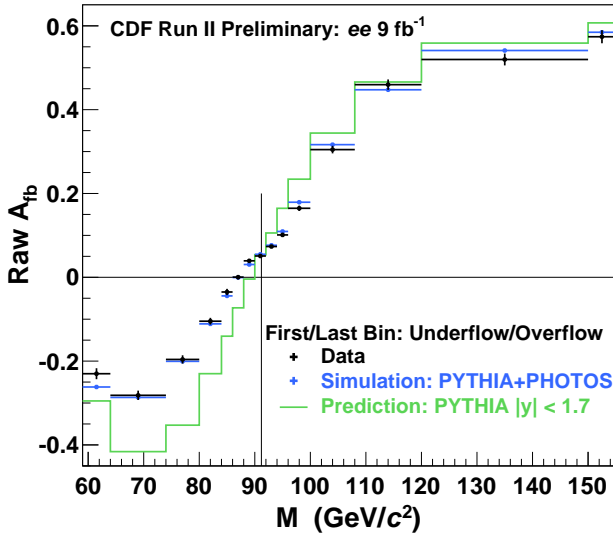


FIG. 13. Raw A_{FB} measurement in bins of the electron-pair invariant mass. The vertical line is at $M = M_Z$. Only statistical uncertainties are shown. The PYTHIA $|y| < 1.7$ asymmetry curve is before QED FSR.

the raw A_{FB} measurement because the event-weighting method provides a first-order acceptance correction, but does not include resolution unfolding and final-state QED radiation. Fifteen mass bins are defined for the the A_{FB} measurement. Their boundaries are 50, 64, 74, 80, 84, 86, 88, 90, 92, 94, 96, 100, 108, 120, 150, and 350 GeV/c^2 . The 50–64 and 150–350 GeV/c^2 bins are referenced as the underflow and overflow bins, respectively. The raw A_{FB} measurement is shown in Fig. 13.

As the CC and CP events have different geometries and resolutions, they are kept separate in the event-weighting phase and the unfolding phase. They are combined for the A_{FB} measurement and calculation of the measurement covariance matrix.

Resolution unfolding uses the event transfer matrices from the simulation, denoted by \bar{n}_{gr} . This symbol identifies the number of selected events that are generated in the electron-pair $(M, \cos\vartheta)$ bin g and reconstructed in the $(M, \cos\vartheta)$ bin r . In addition to the 15 mass bins, the forward-backward asymmetry has two angular regions $\cos\vartheta \geq 0$ (+) and $\cos\vartheta < 0$ (–). Operationally, 30×30 square transfer matrices for a 30-element state vector are implemented. The first 15 elements of the vector are the mass bins for the + angular region, and the remaining 15 elements are for the – angular region.

The simulation predicts significant bin-to-bin event migration among the mass bins when the produced and reconstructed values of $\cos\vartheta$ have the same sign. For a mass bin, there is very little migration of events from one angular region to the other. As the simulation sample size is normalized to the integrated luminosity of the data, the transfer matrices provide properly normalized estimates of event migration between bins. An estimator for the true unfolding matrix is $\bar{U}_{gr} = \bar{n}_{gr}/\bar{N}_r$, where $\bar{N}_r = \sum_g \bar{n}_{gr}$ is the expected total number of weighted events reconstructed in bin r . The 30-element state vector for \bar{N}_r is denoted as \bar{N}_r , and the matrix \bar{U}_{gr} by \mathbf{U} . The estimate for the resolution-unfolded state vector of produced events is $\vec{N}_g = \mathbf{U} \cdot \bar{N}_r$. The accuracy of the simulation of \mathbf{U} is determined by the sample size of the data used for calibrations and corrections.

For the event-weighting method, there are two transfer matrices that correspond to the weighted event counts N_n and N_d of Eq. (5), and thus two separate unfolding matrices \mathbf{U} and two separate event-weighted measurements of \vec{N}_r . They are used to estimate the two resolution-unfolded \vec{N}_g vectors from which A_{FB} is derived. The measurements of A_{FB} for the 15 mass bins are collectively denoted by \vec{A}_{FB} .

The covariance matrix of the A_{FB} measurement, denoted by \mathbf{V} , is calculated using the unfolding matrices, the expectation values of \vec{N}_r and \vec{A}_{FB} from the simulation, and their fluctuations over an ensemble. The per-experiment fluctuation to \vec{N}_g is $\mathbf{U} \cdot (\vec{N}_r + \delta\vec{N}_r)$, where $\delta\vec{N}_r$ represents a fluctuation from the expectation \vec{N}_r . The variation $\delta\vec{A}_{FB}$ resulting from the \vec{N}_g fluctuation is ensemble averaged to obtain the covariance matrix

$$V_{lm} = \langle (\delta\vec{A}_{FB})_l (\delta\vec{A}_{FB})_m \rangle,$$

where $(\delta\vec{A}_{FB})_k$ ($k = l$ and m) denotes the k -th element of $\delta\vec{A}_{FB}$. Each element i of \vec{N}_r receives independent, normally distributed fluctuations with a variance equal to the value expected for \bar{N}_i . Because \bar{N}_i is a sum of event weights, fluctuations of \bar{N}_i are quantified with the variance of its event weights. The two \vec{N}_r vectors, the numerator vector and the denominator vector, have correlations. Elements i of the numerator and denominator vectors contain the same events; the only difference being that they have different event weights. To include this correlation, the event-count variations of elements i of the numerator and denominator $\delta\vec{N}_r$ vectors are based

on the same fluctuation from a normal distribution with unit rms.

The covariance matrix is expanded and inverted to the error matrix using singular-value decomposition (SVD) methods. As the covariance matrix is a real-valued symmetric 15×15 matrix, its 15 eigenvalues and eigenvectors are the rank-1 matrix components in the decomposition of the covariance matrix and the error matrix

$$\mathbf{V} = \sum_n \lambda_n (\vec{v}_n \vec{v}_n) \text{ and } \mathbf{V}^{-1} = \sum_n \lambda_n^{-1} (\vec{v}_n \vec{v}_n),$$

where λ_n and \vec{v}_n are the eigenvalues and eigenvectors of \mathbf{V} , respectively, and $(\vec{v}_n \vec{v}_n)$ represents a vector projection operator, *i.e.*, $|v_n\rangle\langle v_n|$ in the style of Dirac bra-kets.

The covariance matrix has eigenvalues with very small values which are a consequence of the ultra-fine details particular to the simulation. While they contribute very little to the overall structure of the covariance matrix, they completely dominate the error matrix. The fine details of the simulation, measurement, and calculation can be quite different because of the different natures. Consequently, comparisons between the A_{fb} measurement and predictions that use the error matrix are unstable. An SVD method to alleviate this instability is used, and presented in Sec. IX.

D. Event-weighting bias correction

After resolution unfolding, the event-weighted A_{fb} values can have second-order acceptance and reconstruction-efficiency biases. The acceptance bias is from regions of limited boson acceptance, and to a lesser extent, from detector nonuniformities resulting in $(\epsilon A)^+ \neq (\epsilon A)^-$. The rapidity acceptance of electron pairs is shown in Fig. 14. As $|y|$ increases, A_{fb} slowly increases, and this increase is not fully taken into account in the regions of very limited boson acceptance. To limit this bias, the measurement of A_{fb} is restricted to the region $|y| < 1.7$. The electron-pair mass range of the measurement, 50 to 350 GeV/c^2 , corresponds to maximum $|y|$ values of 3.7 to 1.7, respectively.

The bias is defined as the difference between the true value of A_{fb} before QED FSR calculated with PYTHIA and the simulation estimate. The estimate is the value of the resolution-unfolded A_{fb} obtained from the event-weighted simulation. The bias is a mass-bin by mass-bin additive correction to the unfolded A_{fb} measurement, and is shown in Fig. 15. All significant bias corrections are under 8% of the magnitude of A_{fb} and most are 3% or less.

The fully corrected measurement of A_{fb} , including the bias correction, is shown in Fig. 16 and tabulated in Table II.

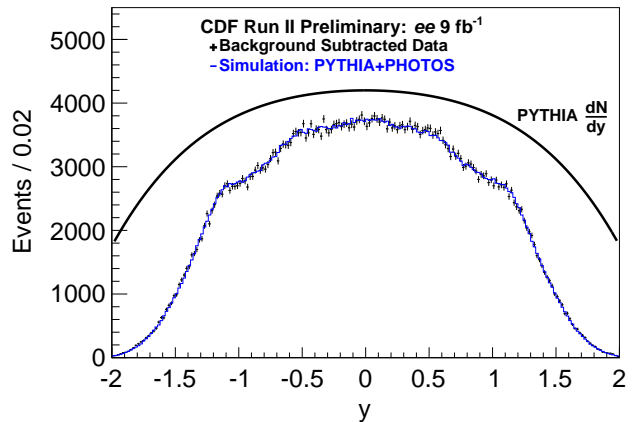


FIG. 14. Rapidity distribution of electron pairs from the CC and CP topologies with $66 < M_{ee} < 116 \text{ GeV}/c^2$. The crosses are the background-subtracted data and the histogram is the simulation. The upper curve is the (arbitrarily normalized) shape of the underlying rapidity distribution from PYTHIA.

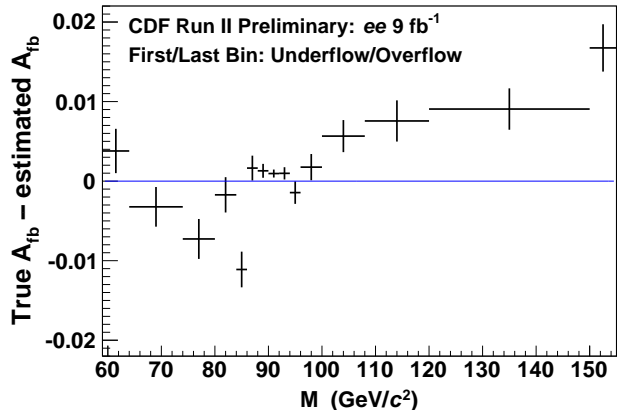


FIG. 15. Event-weighting bias for each of the electron-pair invariant mass bins. The bias is estimated with the simulation, and the uncertainties represent the full precision of the simulation.

IX. EXTRACTION OF $\sin^2 \theta_{\text{eff}}^{\text{lept}}$

The EWK mixing parameters $\sin^2 \theta_{\text{eff}}^{\text{lept}}$ and $\sin^2 \theta_W$ are extracted from the A_{fb} measurement presented in Fig. 16 using A_{fb} templates calculated using different values of $\sin^2 \theta_W$. Three EBA-based calculations are used: LO (tree), RESBOS NLO, and POWHEG-BOX NLO. For the EBA electroweak form-factor calculations, the weak-mixing parameter is $\sin^2 \theta_W$.

The A_{fb} measurement is directly sensitive to the effective-mixing parameters $\sin^2 \theta_{\text{eff}}$, which are combinations of the form factors and $\sin^2 \theta_W$ (Sec. III A). The Drell-Yan A_{fb} is most sensitive to the effective-leptonic $\sin^2 \theta_{\text{eff}}^{\text{lept}}$. While the extracted values of the effective-mixing parameters are independent of the details of the EBA model, the interpretation of the best-fit value of

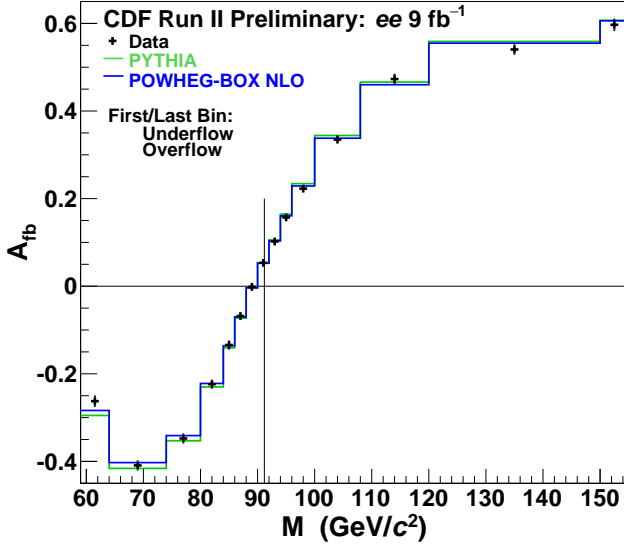


FIG. 16. Fully corrected A_{fb} . The measurement uncertainties are bin-by-bin unfolding estimates. The vertical line is $M = M_Z$. The PYTHIA calculation uses $\sin^2 \theta_{eff}^{lept} = 0.232$. The EBA-based POWHEG-BOX calculation uses $\sin^2 \theta_W = 0.2243$ ($\sin^2 \theta_{eff}^{lept} = 0.2325$) and the default PDF of NNPDF-3.0.

TABLE II. The fully corrected A_{fb} measurement. The measurement uncertainties are uncorrelated bin-by-bin unfolding estimates.

Mass bin (GeV/c ²)	A_{fb}
50–64	-0.262 ± 0.014
64–74	-0.409 ± 0.015
74–80	-0.348 ± 0.015
80–84	-0.224 ± 0.014
84–86	-0.134 ± 0.014
86–88	-0.068 ± 0.010
88–90	0.0015 ± 0.0044
90–92	0.053 ± 0.0017
92–94	0.102 ± 0.0036
94–96	0.157 ± 0.0087
96–100	0.223 ± 0.0094
100–108	0.335 ± 0.010
108–120	0.473 ± 0.012
120–150	0.541 ± 0.012
150–350	0.597 ± 0.014

$\sin^2 \theta_W$ and its corresponding form factors are dependent on the details of the EBA model.

The measurement and templates are compared using the χ^2 statistic evaluated with the A_{fb} measurement error matrix. Each template provides a scan point for the χ^2 function: $(\sin^2 \theta_W, \chi^2(\sin^2 \theta_W))$. The scan points are fit to a parabolic χ^2 function:

$$\chi^2(\sin^2 \theta_W) = \bar{\chi}^2 + (\sin^2 \theta_W - \overline{\sin^2 \theta_W})^2 / \bar{\sigma}^2, \quad (6)$$

where $\bar{\chi}^2$, $\overline{\sin^2 \theta_W}$, and $\bar{\sigma}$ are parameters. The $\overline{\sin^2 \theta_W}$

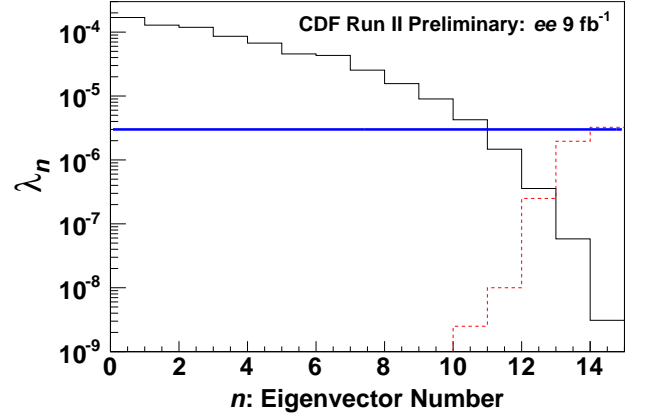


FIG. 17. λ_n : Eigenvalues of the error matrix. The eigenvalues are represented by the solid histogram and the regularization terms by the dashed histogram. The horizontal line is the square of the A_{fb} measurement uncertainty for the mass bin containing the Z peak.

parameter is the best-fit value of $\sin^2 \theta_W$, $\bar{\sigma}$ is the corresponding measurement uncertainty, and $\bar{\chi}^2$ is the associated goodness-of-fit between the A_{fb} measurement and calculation over the 15 mass bins.

Without regularization of the error matrix, there are large fluctuations of each scan point from the expected parabolic form. The SVD regularization function method is chosen to attenuate these fluctuations. A regularization term or function is added to the eigenvalues of the error matrix: $\lambda_n \rightarrow \lambda_n + r_n \equiv \lambda'_n$, where r_n is the regularization term of eigenvector n and λ'_n is the regularized eigenvalue. The eigenvalues and regularization terms are shown in Fig. 17. In the basis vector space of the error matrix, the χ^2 for each scan point becomes $\sum_n (\delta A_{fb})_n^2 / \lambda'_n$, where the index n runs over all the eigenvector numbers and δA_{fb} is the difference between the measured and calculated values of A_{fb} .

The effectiveness of the regularization is measured with the goodness-of-fit between the $\chi^2(\sin^2 \theta_W)$ value of the scan points and the parabolic function. With pseudoinverse regularization, the SVD expansion of the error matrix is truncated. Truncating eigenvectors 13 and 14 from the error matrix significantly improves the goodness-of-fit. The optimized regularization function shown in Fig. 17 is determined as follows. First, the shape of the regularization function is chosen so that it selectively suppresses eigenvectors that project noise rather than the uncertainties of the measurement or calculation, e.g., eigenvectors 13 and 14. Then the optimum normalization level is determined via a scan of level scale-factor values, starting from 0. As the scale-factor value increases, the goodness-of-fit rapidly improves then enters a plateau region without significant improvement and only a degradation of the measurement resolution. The optimum is chosen to be slightly beyond the start of the plateau region where the $\overline{\sin^2 \theta_W}$ parameter is also stable in value.

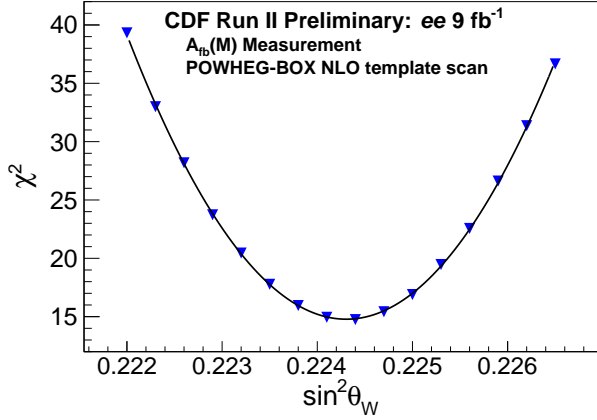


FIG. 18. $\sin^2 \theta_W$ template scan. The triangles are the comparisons of the A_{fb} measurement with the POWHEG-BOX NLO calculations. The A_{fb} templates of each scan point are calculated with the default PDF of NNPDF-3.0. The solid curve is the fit of those points to the χ^2 parabolic function.

The basic steps in the extraction of $\sin^2 \theta_W$ are summarized below. Templates of \vec{A}_{fb} are calculated for a series of $\sin^2 \theta_W$ scan points, and the χ^2 between the measurement and calculated \vec{A}_{fb} is evaluated with the error matrix of the measurement. As the χ^2 with the unmodified error matrix is unstable with respect to fluctuations, the error matrix is regulated with the function shown in Fig. 17. The scan points are fit to Eq. 6 for the determination of the best-fit $\sin^2 \theta_W$. An example of the template scan extraction of $\sin^2 \theta_W$ is shown in Fig. 18.

The EBA-based tree and POWHEG-BOX NLO calculations of A_{fb} use NNPDF-3.0 PDFs, an ensemble of probability-based PDFs. Such ensembles are samples from the entire probability density function of measurement-constrained PDFs [40]. For these ensembles, the predicted value of A_{fb} is the average of values calculated over the sample distribution where the calculation for each sample is weighted with its probability. The rms of the average over the sample distribution is the PDF uncertainty.

The NNPDF-3.0 ensemble consists of 100 equally probable samples. The best-fit parameters of template scans based on each of the ensemble PDFs, $\overline{\sin^2 \theta_W}$, $\overline{\chi^2}$ and $\overline{\sigma}$, are derived, then averaged. The results of the EBA-based POWHEG-BOX calculations of A_{fb} is used as the central value of $\sin^2 \theta_W$. The results of the template scans are summarized in Table III. Included in the table for comparison are these measurements: the CDF 2.1 fb $^{-1}$ ee -pair A_4 result [4], the CDF 9.2 fb $^{-1}$ $\mu\mu$ -pair A_{fb} results [4], and standard model Z -pole fits from LEP-1 and SLD [8]; the uncertainties of these measurements are the full uncertainties. The CDF measurements use EBA-based QCD calculations to indirectly determine $\sin^2 \theta_W$.

The $\overline{\chi^2}$ values listed in Table III indicate that the POWHEG-BOX calculation provides the best description

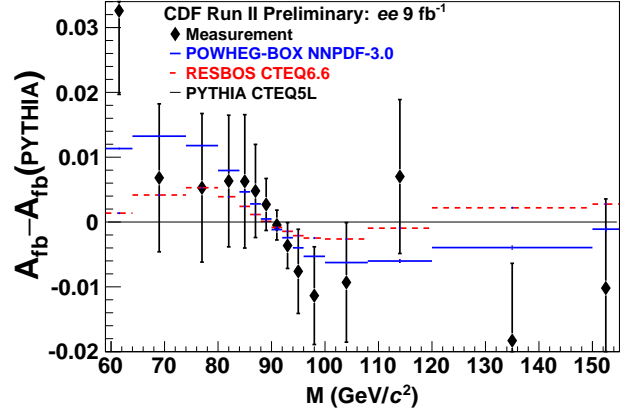


FIG. 19. $\Delta A_{fb} \equiv A_{fb} - A_{fb}(\text{PYTHIA})$. The diamonds represent the measurement and uncertainties shown are the bin-by-bin unfolding estimates which are highly correlated in the vicinity of the Z -boson mass. The solid bars represent the POWHEG-BOX template calculated with the default NNPDF-3.0 PDFs. The dashed bars represent the RESBOS template calculated with CTEQ6.6 PDFs. Both calculations use $\sin^2 \theta_W = 0.2243$. The horizontal line represents the reference PYTHIA calculation which uses CTEQ5L PDFs with $\sin^2 \theta_{\text{eff}}^{\text{lept}} = 0.232$.

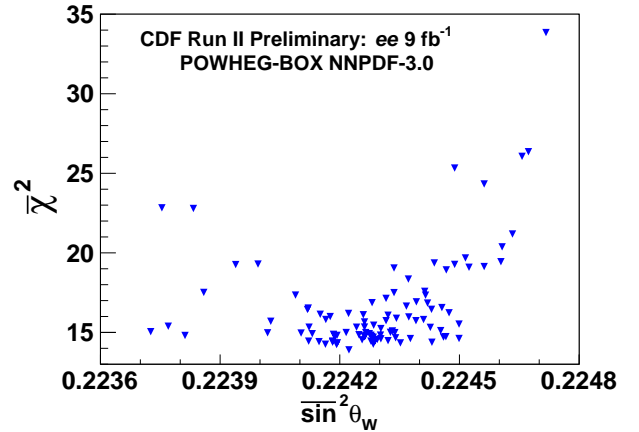


FIG. 20. $\overline{\chi^2}$ versus $\overline{\sin^2 \theta_W}$ parameters for the fits with PDFs of the NNPDF-3.0 ensemble. The A_{fb} measurement and templates span 15 mass bins.

of the A_{fb} measurement. For graphical comparisons of best-fit A_{fb} templates, the difference relative to a reference calculation is used: $\Delta A_{fb} \equiv A_{fb} - A_{fb}(\text{PYTHIA})$ where the reference $A_{fb}(\text{PYTHIA})$ is the tuned PYTHIA calculation described in Sec. VI on the signal simulation. Figure 19 shows the ΔA_{fb} distributions of the measurement, the POWHEG-BOX calculation, and the RESBOS calculation. Figure 20 shows the relationship of the $\overline{\chi^2}$ and $\overline{\sin^2 \theta_W}$ fit parameters for the PDFs of the NNPDF-3.0 ensemble. This is a direct illustration of the consistency of the A_{fb} measurement with the measurements used to constrain the PDFs of the NNPDF-3.0 ensemble.

TABLE III. Extracted values of $\sin^2 \theta_{\text{eff}}^{\text{lept}}$ and $\sin^2 \theta_W$ for the EBA-based QCD templates. The PYTHIA entry is the value from the scan over non-EBA templates calculated by PYTHIA 6.4 with CTEQ5L PDFs. The uncertainties of the template scans are the measurement uncertainties ($\bar{\sigma}$). For the $\bar{\chi}^2$ column, the number in parenthesis is the number of mass bins of the A_{fb} measurement. Other measurements are listed in parentheses.

Template (Measurement)	$\sin^2 \theta_{\text{eff}}^{\text{lept}}$	$\sin^2 \theta_W$	$\bar{\chi}^2$
POWHEG-BOX NLO	0.23249 ± 0.00048	0.22429 ± 0.00046	16.6 (15)
RESBOS NLO	0.23249 ± 0.00048	0.22429 ± 0.00046	22.4 (15)
Tree LO	0.23252 ± 0.00048	0.22432 ± 0.00046	23.4 (15)
PYTHIA	0.23207 ± 0.00045	—	20.8 (15)
(CDF 9.2 fb $^{-1}$ $A_{\text{fb}}^{(\mu\mu)}$)	0.2315 ± 0.0010	0.2233 ± 0.0009	21.1 (16)
(CDF 2.1 fb $^{-1}$ $A_4^{(ee)}$)	0.2328 ± 0.0010	0.2246 ± 0.0009	—
(LEP-1 and SLD $A_{\text{FB}}^{0,b}$)	0.23221 ± 0.00029	—	—
(SLD \mathcal{A}_ℓ)	0.23098 ± 0.00026	—	—

X. SYSTEMATIC UNCERTAINTIES

The systematic uncertainties contain contributions from both the measurement of A_{fb} and the template predictions of A_{fb} for various input values of $\sin^2 \theta_W$. Both the experimental and prediction-related systematic uncertainties are small compared to the experimental statistical uncertainty. The A_{fb} templates from the EBA-based POWHEG-BOX calculations are used to estimate systematic uncertainties on the $\sin^2 \theta_W$ parameter from various sources.

A. Measurement

The uncertainties considered are from the energy scale and from the background estimates. For the propagation of uncertainties to the extracted value of $\sin^2 \theta_W$, the default PDF of the NNPDF-3.0 ensemble is used. The total measurement systematic uncertainty is ± 0.00003 .

The reconstruction-level energy scale of both the data and simulation are calibrated with the same technique to the underlying-physics scale. The energy-scale systematic uncertainty investigated is from a relative offset between the scales of the data and simulation. The global energy-momentum scale of the simulation is varied to determine the relative shifts allowed by the Z -pole mass constraint in the electron-pair invariant-mass distributions of the experimental and simulated data. Scale shifts for the central and plug EM calorimeters are considered separately. The resulting systematic uncertainty from the energy scale is ± 0.00003 .

For the background systematic uncertainty, the normalization uncertainties of the two largest backgrounds, QCD and $Z \rightarrow \tau\tau$, are considered. They amount to three-quarters of the total background. The uncertainty of their normalization levels from the background fits described in Sec. VII C is propagated into an uncertainty for $\sin^2 \theta_W$. For the $Z \rightarrow \tau\tau$ background of the CC topology, the difference between the constrained and unconstrained fit levels, is assigned as a systematic uncertainty; this is

the dominant uncertainty. The resulting systematic uncertainty from the backgrounds is ± 0.00002 .

B. Predictions

The uncertainties considered are from the PDFs, the QCD mass-factorization and renormalization scales, and higher-order QCD effects. The total prediction uncertainty is ± 0.00020 .

The PDF uncertainty of the central value of the extracted $\sin^2 \theta_W$ value shown in Table III for the POWHEG-BOX NLO entry is ± 0.00020 . This is the rms of the ensemble average for NNPDF-3.0.

In all of the POWHEG-BOX calculations, the QCD mass-factorization and renormalization scales are set to the electron-pair invariant mass. To evaluate the effects of different scales, the running scales are varied independently by a factor ranging from 0.5 to 2 in the calculations. For the calculation of templates used to evaluate the scale uncertainty, the default PDF of the NNPDF-3.0 ensemble is used. The rms of the best-fit value of $\sin^2 \theta_W$ based on different scales relative to the default scale is assigned as the QCD-scale uncertainty. This uncertainty is ± 0.00001 .

The uncertainty of higher-order QCD effects is estimated with the difference between the values of $\sin^2 \theta_W$ in Table III extracted with the tree and POWHEG-BOX NLO templates. Both template calculations are EBA based and use the NNPDF-3.0 PDF ensemble. This uncertainty, denoted as the QCD EBA uncertainty, is ± 0.00003 . Although the POWHEG-BOX prediction is a fixed-order NLO QCD calculation at large boson P_T , it is an all-orders resummation calculation in the low-to-moderate P_T region, which provides most of the total cross section.

TABLE IV. Summary of the systematic uncertainties on the extraction of the weak mixing parameters $\sin^2 \theta_{\text{eff}}^{\text{lept}}$ and $\sin^2 \theta_W$.

Source	$\sin^2 \theta_{\text{eff}}^{\text{lept}}$	$\sin^2 \theta_W$
Energy scale	± 0.00003	± 0.00003
Backgrounds	± 0.00002	± 0.00002
QCD scales	± 0.00001	± 0.00001
NNPDF-3.0 PDF	± 0.00020	± 0.00020
QCD EBA	± 0.00003	± 0.00003

XI. RESULTS

The values for $\sin^2 \theta_{\text{eff}}^{\text{lept}}$ and $\sin^2 \theta_W$ (M_W) extracted from the measurement of A_{FB} using e^+e^- pairs from a sample corresponding to 9.4 fb^{-1} are

$$\sin^2 \theta_{\text{eff}}^{\text{lept}} = 0.23249 \pm 0.00048 \pm 0.00021$$

$$\sin^2 \theta_W = 0.22429 \pm 0.00046 \pm 0.00020$$

$$M_W (\text{indirect}) = 80.313 \pm 0.024 \pm 0.010 \text{ GeV}/c^2,$$

where the first contribution to the uncertainties is statistical and the second is systematic. All systematic uncertainties are combined in quadrature, and the sources and values of these uncertainties are summarized in Table IV. The inferred result on $\sin^2 \theta_W$ or M_W is dependent on the standard model context specified in the appendix. The $\sin^2 \theta_{\text{eff}}^{\text{lept}}$ result is independent because of its direct relationship with A_{FB} .

The measurement of $\sin^2 \theta_{\text{eff}}^{\text{lept}}$ is compared with previous results from the Tevatron, LHC, LEP-1, and SLD in Fig. 21. The Tevatron results from CDF [4] and D0 [5] are based on A_{FB} measurements. The LHC results from ATLAS [6] and CMS [7] are based on A_{FB} measurements as well. The LEP-1 and SLD results are from measurements at the Z -pole. The Z -pole value is the combination of the following six measurements [8].

$$A_{\text{FB}}^{0,\ell} \rightarrow 0.23099 \pm 0.00053$$

$$\mathcal{A}_\ell(P_\tau) \rightarrow 0.23159 \pm 0.00041$$

$$\mathcal{A}_\ell(\text{SLD}) \rightarrow 0.23098 \pm 0.00026$$

$$A_{\text{FB}}^{0,b} \rightarrow 0.23221 \pm 0.00029$$

$$A_{\text{FB}}^{0,c} \rightarrow 0.23220 \pm 0.00081$$

$$Q_{\text{FB}}^{\text{had}} \rightarrow 0.2324 \pm 0.0012$$

The $Q_{\text{FB}}^{\text{had}}$ measurement is based on the hadronic charge-asymmetry of all hadronic events.

The W -boson mass inference is compared in Fig. 22 with previous direct and indirect measurements from the Tevatron, NuTeV, LEP-1, SLD, and LEP-2. The direct measurement is from the Tevatron and LEP-2 [42]. The indirect measurement from the Tevatron is derived from the CDF measurement of A_{FB} with muon pairs and it uses the same EBA-based method of inference. The indirect measurement from LEP-1 and SLD is from electroweak

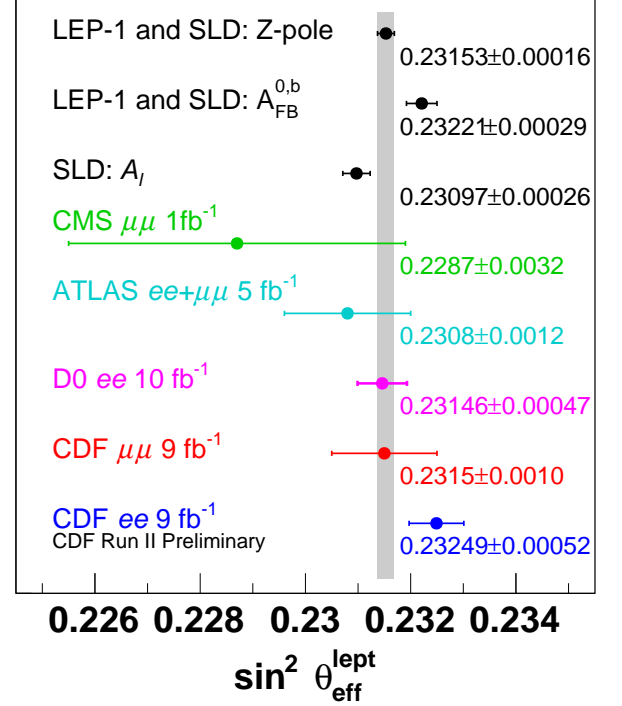


FIG. 21. Comparison of experimental measurements of $\sin^2 \theta_{\text{eff}}^{\text{lept}}$. This measurement is denoted as “CDF ee 9 fb^{-1} ” and the others are previous measurements described in the text. The combination of the six LEP-1 and SLD Z -pole measurements is denoted as “ Z -pole”. The horizontal bars represent total uncertainties.

standard model fits to Z -pole measurements in combination with the Tevatron top-quark mass measurement [43]. The NuTeV value, an indirect measurement, is based on the on-shell $\sin^2 \theta_W$ parameter extracted from the measurement of the ratios of the neutral-to-charged current ν and $\bar{\nu}$ cross sections at Fermilab [9].

XII. SUMMARY

The angular distribution of Drell-Yan lepton pairs provides information on the electroweak-mixing parameter $\sin^2 \theta_W$. The electron forward-backward asymmetry in the polar-angle distribution $\cos \vartheta$ is governed by the $A_4 \cos \vartheta$ term, whose A_4 coefficient is directly related to the $\sin^2 \theta_{\text{eff}}^{\text{lept}}$ mixing parameter at the lepton vertex, and indirectly to $\sin^2 \theta_W$. The effective-leptonic parameter $\sin^2 \theta_{\text{eff}}^{\text{lept}}$ is derived from the measurement of the forward-backward asymmetry $A_{\text{FB}}(M)$ based on the entire CDF Run II sample of electron pairs, which corresponds to 9.4 fb^{-1} of integrated luminosity from $p\bar{p}$ collisions at a center-of-momentum energy of 1.96 TeV. Calculations of $A_{\text{FB}}(M)$ with different values of the electroweak-mixing parameter are compared with the measurement to determine the value of the parameter that best describes the

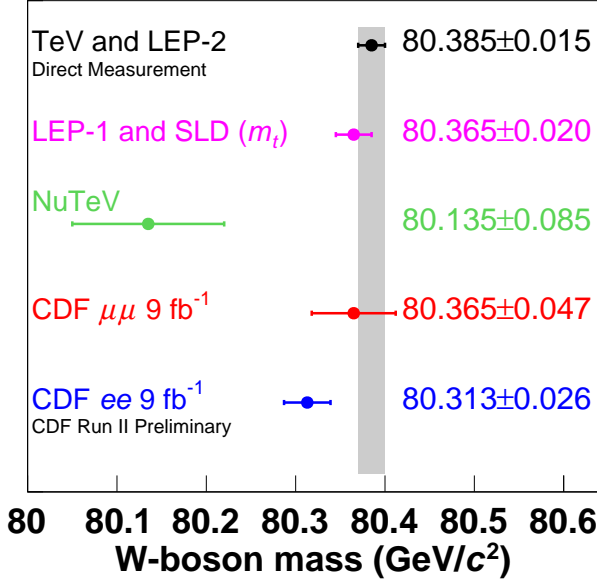


FIG. 22. Comparison of experimental determinations of the W -boson mass. The direct measurement is denoted by “TeV and LEP-2” and the others are indirect measurements. This measurement is denoted by “CDF ee 9 fb $^{-1}$ ” and the others are described in the text. The horizontal bars represent total uncertainties.

data. The calculations include both quantum chromodynamic and electroweak radiative corrections. The best-fit values from the comparisons are summarized as follows:

$$\begin{aligned}\sin^2 \theta_{\text{eff}}^{\text{lept}} &= 0.23249 \pm 0.00052 \\ \sin^2 \theta_W &= 0.22429 \pm 0.00050 \\ M_W(\text{indirect}) &= 80.313 \pm 0.026 \text{ GeV}/c^2.\end{aligned}$$

Each uncertainty includes statistical and systematic contributions. Both results are consistent with LEP-1 and SLD measurements at the Z -boson pole. The value of $\sin^2 \theta_{\text{eff}}^{\text{lept}}$ is also consistent with the previous results from the Tevatron [4, 5].

Appendix: ZFITTER

The input parameters to the ZFITTER radiative-correction calculation are particle masses, the electromagnetic fine-structure constant α_{em} , the Fermi constant G_F , the strong-interaction coupling at the Z mass $\alpha_s(M_Z^2)$, and the contribution of the light quarks to the “running” α_{em} at the Z mass $\Delta\alpha_{em}^{(5)}(M_Z^2)$ (DALH5). The scale-dependent couplings are $\alpha_s(M_Z^2) = 0.118$ and $\Delta\alpha_{em}^{(5)}(M_Z^2) = 0.0275$ [44]. The mass parameters are $M_Z = 91.1875 \text{ GeV}/c^2$ [8], $m_t = 173.2 \text{ GeV}/c^2$ (top quark) [43], and $m_H = 125 \text{ GeV}/c^2$ (Higgs boson). Form factors and the Z -boson total decay-width Γ_Z are calculated.

The renormalization scheme used by ZFITTER is the on-shell scheme [14], where particle masses are on-shell and

$$\sin^2 \theta_W = 1 - M_W^2/M_Z^2 \quad (\text{A.1})$$

holds to all orders of perturbation theory by definition. If both G_F and m_H are specified, $\sin \theta_W$ is not independent, and it is derived from standard model constraints that use radiative corrections. To vary the $\sin \theta_W$ (M_W) parameter, the value of G_F is changed by a small amount prior to the calculation so that the derived M_W range is 80.0–80.5 GeV/ c^2 . The set of resulting M_W values corresponds to a family of physics models with standard model like couplings where $\sin^2 \theta_W$ and the coupling (G_F) are defined by the M_W parameter. The Higgs-boson mass constraint $m_H = 125 \text{ GeV}/c^2$ keeps the form factors within the vicinity of standard model fit values from LEP-1 and SLD [8].

The primary purpose of ZFITTER is to provide tables of form factors for each model. As the form factors are calculated in the massless-fermion approximation, they only depend on the fermion weak isospin and charge, and are distinguished via three indices: e (electron type), u (up-quark type), and d (down-quark type).

For the $ee \rightarrow Z \rightarrow q\bar{q}$ process, the ZFITTER scattering-amplitude ansatz is

$$\begin{aligned}A_q &= \frac{i}{4} \frac{\sqrt{2}G_F M_Z^2}{\hat{s} - (M_Z^2 - i\hat{s}\Gamma_Z/M_Z)} 4T_3^e T_3^q \rho_{eq} \\ &\quad [\langle \bar{e} | \gamma^\mu (1 + \gamma_5) | e \rangle \langle \bar{q} | \gamma_\mu (1 + \gamma_5) | q \rangle + \\ &\quad -4|Q_e| \kappa_e \sin^2 \theta_W \langle \bar{e} | \gamma^\mu | e \rangle \langle \bar{q} | \gamma_\mu (1 + \gamma_5) | q \rangle + \\ &\quad -4|Q_q| \kappa_q \sin^2 \theta_W \langle \bar{e} | \gamma^\mu (1 + \gamma_5) | e \rangle \langle \bar{q} | \gamma_\mu | q \rangle + \\ &\quad 16|Q_e Q_q| \kappa_{eq} \sin^4 \theta_W \langle \bar{e} | \gamma^\mu | e \rangle \langle \bar{q} | \gamma_\mu | q \rangle],\end{aligned}$$

where $q = u$ or d , the ρ_{eq} , κ_e , κ_q , and κ_{eq} are complex-valued form factors, the bilinear γ matrix terms are covariantly contracted, and $\frac{1}{2}(1 + \gamma_5)$ is the left-handed helicity projector in the ZFITTER convention. The κ_e form factors of the A_u and A_d amplitudes are not equivalent; however, at $\hat{s} = M_Z^2$, they are numerically equal.

The ρ_{eq} , κ_e , and κ_q form factors are incorporated into QCD calculations as corrections to the Born-level g_A^f and g_V^f couplings:

$$\begin{aligned}g_V^f &\rightarrow \sqrt{\rho_{eq}} (T_3^f - 2Q_f \kappa_f \sin^2 \theta_W) \text{ and} \\ g_A^f &\rightarrow \sqrt{\rho_{eq}} T_3^f,\end{aligned}$$

where $f = e$ or q . The resulting current-current amplitude is similar to A_q , but the $\sin^4 \theta_W$ term contains $\kappa_e \kappa_q$. The difference is removed with the addition of this amplitude correction: the $\sin^4 \theta_W$ term of A_q with $\kappa_{eq} \rightarrow \kappa_{eq} - \kappa_e \kappa_q$. Implementation details are provided in Ref. [4].

-
- [1] S. D. Drell and T.-M. Yan, Phys. Rev. Lett. **25**, 316 (1970).
- [2] J. Beringer *et al.* (Particle Data Group), Phys. Rev. D **86**, 010001 (2012), and 2013 partial update for the 2014 edition.
- [3] D. Acosta *et al.* (CDF Collaboration), Phys. Rev. D **71**, 052002 (2005).
- [4] T. Aaltonen *et al.* (CDF Collaboration), Phys. Rev. D **88**, 072002 (2013); Phys. Rev. D **88**, 079905(E) (2013); Phys. Rev. D **89**, 072005 (2014).
- [5] V. M. Abazov *et al.* (D0 Collaboration), Phys. Rev. Lett. **115**, 041801 (2015); Phys. Rev. D **84**, 012007 (2011).
- [6] G. Aad *et al.* (ATLAS Collaboration), Submitted to JHEP (2015), arXiv:1503.03709 [hep-ex].
- [7] S. Chatrchyan *et al.* (CMS Collaboration), Phys. Rev. D **84**, 112002 (2011).
- [8] S. Schael *et al.* (ALEPH, DELPHI, L3, OPAL, and SLD Collaborations, LEP Electroweak Working Group, and SLD Electroweak and Heavy Flavour Groups), Phys. Rept. **427**, 257 (2006).
- [9] G. P. Zeller *et al.* (NuTeV Collaboration), Phys. Rev. Lett. **88**, 091802 (2002); Phys. Rev. Lett. **90**, 239902(E) (2003).
- [10] A. Aktas *et al.* (H1 Collaboration), Phys. Lett. B **632**, 35 (2006).
- [11] J. C. Collins and D. E. Soper, Phys. Rev. D **16**, 2219 (1977).
- [12] E. Mirkes, Nucl. Phys. **B387**, 3 (1992); E. Mirkes and J. Ohnemus, Phys. Rev. D **50**, 5692 (1994).
- [13] D. Bardin, M. Bilenky, T. Riemann, M. Sachwitz, and H. Vogt, Comput. Phys. Commun. **59**, 303 (1990); D. Bardin, P. Christova, M. Jack, L. Kalinovskaya, A. Olchevski, S. Riemann, and T. Riemann, Comput. Phys. Commun. **133**, 229 (2001); A. Arbuzov, M. Awramik, M. Czakon, A. Freitas, M. Grünewald, K. Monig, S. Riemann, and T. Riemann, Comput. Phys. Commun. **174**, 728 (2006).
- [14] A. Sirlin, Phys. Rev. D **22**, 971 (1980).
- [15] P. M. Nadolsky *et al.* (CTEQ Collaboration), Phys. Rev. D **78**, 103004 (2008).
- [16] R. D. Ball *et al.* (NNPDF Collaboration), J. High Energy Phys. **04**, 040 (2015); Nucl. Phys. **B867**, 244 (2013); R. D. Ball, V. Bertone, F. Cerutti, L. D. Debbio, S. Forte, A. Guffanti, J. I. Latorre, J. Rojo, and M. Ubiali (NNPDF Collaboration), Nucl. Phys. **B855**, 153 (2012); Nucl. Phys. **B849**, 296 (2011); R. D. Ball, L. D. Debbio, S. Forte, A. Guffanti, J. I. Latorre, J. Rojo, and M. Ubiali (NNPDF Collaboration), Nucl. Phys. **B838**, 136 (2010); R. D. Ball, L. D. Debbio, S. Forte, A. Guffanti, J. I. Latorre, A. Piccione, J. Rojo, and M. Ubiali (NNPDF Collaboration), Nucl. Phys. **B809**, 1 (2009); Nucl. Phys. **B816**, 293 (2009); S. Forte, L. Garrido, J. I. Latorre, and A. Piccione, J. High Energy Phys. **05**, 062 (2002).
- [17] G. A. Ladinsky and C.-P. Yuan, Phys. Rev. D **50**, R4239 (1994); C. Balázs and C.-P. Yuan, Phys. Rev. D **56**, 5558 (1997); F. Landry, R. Brock, P. M. Nadolsky, and C.-P. Yuan, Phys. Rev. D **67**, 073016 (2003); A. Konychev and P. Nadolsky, Phys. Lett. B **633**, 710 (2006).
- [18] S. Alioli, P. Nason, C. Oleari, and E. Re, J. High Energy Phys. **07**, 060 (2008).
- [19] J. C. Collins, D. E. Soper, and G. Sterman, Nucl. Phys. **B250**, 199 (1985); J. C. Collins and D. E. Soper, Nucl. Phys. **B193**, 381 (1981); Nucl. Phys. **B197**, 446 (1982); Nucl. Phys. **B213**, 545(E) (1983).
- [20] V. V. Sudakov, Sov. Phys. JETP **3**, 65 (1956); Zh. Eksp. Teor. Fiz. **30**, 87 (1956).
- [21] T. Sjöstrand, S. Mrenna, and P. Z. Skands, J. High Energy Phys. **05**, 026 (2006).
- [22] A. Abulencia *et al.* (CDF Collaboration), J. Phys. G: Nucl. Part. Phys. **34**, 2457 (2007).
- [23] T. Affolder *et al.*, Nucl. Instrum. Methods Phys. Res., Sect. A **526**, 249 (2004).
- [24] T. Aaltonen *et al.*, Nucl. Instrum. Methods Phys. Res., Sect. A **729**, 153 (2013).
- [25] L. Balka *et al.*, Nucl. Instrum. Methods Phys. Res., Sect. A **267**, 272 (1988).
- [26] S. Bertolucci *et al.*, Nucl. Instrum. Methods Phys. Res., Sect. A **267**, 301 (1988).
- [27] M. Albrow *et al.*, Nucl. Instrum. Methods Phys. Res., Sect. A **480**, 524 (2002).
- [28] G. Apollinari *et al.*, Nucl. Instrum. Methods Phys. Res., Sect. A **412**, 515 (1998).
- [29] P. de Barbaro, IEEE Trans. Nucl. Sci. **42**, 510 (1995).
- [30] T. Aaltonen *et al.* (CDF Collaboration), Phys. Rev. Lett. **106**, 241801 (2011).
- [31] T. Sjöstrand, P. Edén, L. Lönnblad, G. Miu, S. Mrenna, and E. Norrbin, Comput. Phys. Commun. **135**, 238 (2001).
- [32] H. L. Lai *et al.* (CTEQ Collaboration), Eur. Phys. J. C **12**, 375 (2000).
- [33] T. Affolder *et al.* (CDF Collaboration), Phys. Rev. Lett. **84**, 845 (2000).
- [34] M. Albrow *et al.* (Tev4LHC QCD Working Group), arXiv:hep-ph/0610012.
- [35] G. Grindhammer, M. Rudowicz, and S. Peters, Nucl. Instrum. Methods Phys. Res., Sect. A **290**, 469 (1990).
- [36] E. Barberio and Z. Was, Computer Phys. Comm. **79**, 291 (1994); E. Barberio, B. van Eijk, and Z. Was, Computer Phys. Comm. **66**, 115 (1991).
- [37] P. Golonka and Z. Was, Eur. Phys. J. C **45**, 97 (2006).
- [38] A. Bodek, A. van Dyne, J.-Y. Han, W. Sakumoto, and A. Strelnikov, Eur. Phys. J. C **72**, 2194 (2012).
- [39] A. Bodek, Eur. Phys. J. C **67**, 321 (2010).
- [40] W. T. Giele and S. Keller, Phys. Rev. D **58**, 094023 (1998).
- [41] N. Sato, J. F. Owens, and H. Prosper, Phys. Rev. D **89**, 114020 (2014).
- [42] T. Aaltonen *et al.* (CDF and D0 Collaboration), Phys. Rev. D **88**, 052018 (2013).
- [43] T. Aaltonen *et al.* (CDF and D0 Collaborations), Phys. Rev. D **86**, 092003 (2012).
- [44] F. Jegerlehner, Nuovo Cim. C **034S1**, 31 (2011).